

Natural ventilation assessment in typical open an semi-open urban environments under various wind directions

Article

Accepted Version

Hang, J., Luo, Z., Sandberg, M. and Jian, G. (2013) Natural ventilation assessment in typical open an semi-open urban environments under various wind directions. *Building and Environment*, 70. pp. 318-333. ISSN 0360-1323 doi: <https://doi.org/10.1016/j.buildenv.2013.09.002> Available at <http://centaur.reading.ac.uk/34361/>

It is advisable to refer to the publisher's version if you intend to cite from the work.

To link to this article DOI: <http://dx.doi.org/10.1016/j.buildenv.2013.09.002>

Publisher: Elsevier

All outputs in CentAUR are protected by Intellectual Property Rights law, including copyright law. Copyright and IPR is retained by the creators or other copyright holders. Terms and conditions for use of this material are defined in the [End User Agreement](#).

www.reading.ac.uk/centaur

CentAUR

Central Archive at the University of Reading

Reading's research outputs online

Accepted Manuscript

Natural ventilation assessment in typical open and semi-open urban environments under various wind directions

Jian Hang, Zhiwen Luo, Mats Sandberg, Jian Gong



PII: S0360-1323(13)00260-6

DOI: [10.1016/j.buildenv.2013.09.002](https://doi.org/10.1016/j.buildenv.2013.09.002)

Reference: BAE 3509

To appear in: *Building and Environment*

Received Date: 20 June 2013

Revised Date: 2 September 2013

Accepted Date: 5 September 2013

Please cite this article as: Hang J, Luo Z, Sandberg M, Gong J, Natural ventilation assessment in typical open and semi-open urban environments under various wind directions, *Building and Environment* (2013), doi: 10.1016/j.buildenv.2013.09.002.

This is a PDF file of an unedited manuscript that has been accepted for publication. As a service to our customers we are providing this early version of the manuscript. The manuscript will undergo copyediting, typesetting, and review of the resulting proof before it is published in its final form. Please note that during the production process errors may be discovered which could affect the content, and all legal disclaimers that apply to the journal pertain.

>Semi-open street roofs protect pedestrians from strong sunshine and heavy rains. >But they may affect airflows and ventilation in urban canopy layers (UCL).> Age of air & flow rates are analyzed under wind directions of $0^\circ, 15^\circ, 30^\circ, 45^\circ$.> Walls fully or partly covering street roofs at $z=H$ get the worst UCL ventilation.> Semi-open street roofs at $z=1.2H, 1.1H$ get good ventilation and are realistic designs.

1 To be resubmitted to Building and Environment, September 2013

2 **Natural ventilation assessment in typical open and semi-open urban**
3 **environments under various wind directions**

4
5 Jian Hang^{a*}, Zhiwen Luo^b, Mats Sandberg^c, Jian Gong^d

6
7 ^aDepartment of Atmospheric Sciences, School of Environmental Science and Engineering, Sun
8 Yat-Sen University, Guangzhou, Guangdong, P. R. China

9 ^b School of Construction Management and Engineering, University of Reading, Reading, UK

10 ^c Laboratory of Ventilation and Air Quality, University of Gävle, SE-80176 Gävle, Sweden

11 ^dSchool of Civil Engineering and Architecture, Nanchang Hangkong University, Nanchang,
12 Jiangxi, 330063, P. R. China

13
14 *Corresponding author. Jian Hang

15 Tel: +86-20-84110375; fax: +86-20-84110375

16 E-mail address: hangj3@mail.sysu.edu.cn

17
18 **Abstract**

19 Semi-open street roofs protect pedestrians from intense sunshine and rains. Their effects on
20 natural ventilation of urban canopy layers (UCL) are less understood. This paper investigates two
21 idealized urban models consisting of 4(2×2) or 16(4×4) buildings under a neutral atmospheric
22 condition with parallel (0°) or non-parallel (15°,30°,45°) approaching wind. The aspect ratio
23 (building height (H) / street width (W)) is 1 and building width is $B=3H$. Computational fluid
24 dynamic (CFD) simulations were first validated by experimental data, confirming that standard
25 $k-\varepsilon$ model predicted airflow velocity better than RNG $k-\varepsilon$ model, realizable $k-\varepsilon$ model and
26 Reynolds stress model. Three ventilation indices were numerically analyzed for ventilation
27 assessment, including flow rates across street roofs and openings to show the mechanisms of air
28 exchange, age of air to display how long external air reaches a place after entering UCL, and
29 purging flow rate to quantify the net UCL ventilation capacity induced by mean flows and
30 turbulence.

31 Five semi-open roof types are studied: Walls being hung above street roofs (coverage
32 ratio $\lambda_a=100\%$) at $z=1.5H$, $1.2H$, $1.1H$ ('Hung1.5H', 'Hung1.2H', 'Hung1.1H' types); Walls partly
33 covering street roofs ($\lambda_a=80\%$) at $z=H$ ('Partly-covered' type); Walls fully covering street roofs
34 ($\lambda_a=100\%$) at $z=H$ ('Fully-covered' type). They basically obtain worse UCL ventilation than open
35 street roof type due to the decreased roof ventilation. 'Hung1.1H', 'Hung1.2H', 'Hung1.5H' types
36 are better designs than 'Fully-covered' and 'Partly-covered' types. Greater urban size contains
37 larger UCL volume and requires longer time to ventilate. The methodologies and ventilation
38 indices are confirmed effective to quantify UCL ventilation.

39

40 **Key words:** Semi-open street roof; natural ventilation; age of air; purging flow rate; CFD
41 simulations; wind tunnel experiment

42

43 1. Introduction

44 Wind from rural areas provides cleaner rural air into urban canopy layers (UCL) to help
45 pollutant and heat dilution. Good UCL ventilation has been known as one of the possible
46 mitigation solutions to improve urban air environments [1-11], meanwhile ameliorate indoor air
47 quality through building ventilation systems.

48 Complemented by wind tunnel/field experiments, computational fluid dynamics (CFD)
49 simulations have been widely used to predict turbulent airflow, mass transports and energy
50 budgets within, close to and above different UCLs [2,4-11, 17-26, 28-37], ranging from street
51 canyons, street intersections, cavities and courtyards, up to structured building arrays and
52 realistic urban areas. Good reviews on this topic can be found in the literatures [12-15]. For two-
53 dimensional (2D) street canyons [1, 15-19], street aspect ratio (building height/street width, H/W)
54 is the first key parameter to affect the flow regimes and pollutant dispersion. For three-
55 dimensional (3D) urban canopy layers, total street length or urban size [8,11,30], building
56 packing density and frontal area density [8,10,20-23], ambient wind directions [23-24, 32, 37],
57 building layouts and height variations [8, 21-23, 25-26] etc, are significant parameters and have
58 been widely investigated.

59 In addition to the widely studied urban models with open street roofs, semi-open street roof
60 is one of popular urban design elements existing in the realistic urban areas to protect pedestrians
61 from strong sunshine and reduce the inconveniences in rainy or snowy days. Such semi-open

62 street roofs have been reported and investigated by experiments and CFD simulations in the
63 literatures [5-7], including a large naturally ventilated semi-open market building [5], a semi-
64 open shopping mall being located in Lisbon, Portugal [6], enclosed-arcade (or semi-open)
65 markets of Korea with eleven arcade-type designs (or semi-open street roof) [7]. Although the
66 requirements of design are different according to various climate conditions, sufficient natural
67 UCL ventilation has been considered as an important environment design factor for more healthy
68 semi-open outdoor environments [5-7]. Fig. 1 shows two other kinds of semi-open street roof
69 designs in the suburb of Guangzhou China, which are located in a subtropical region annually
70 characterized by intense solar radiation and precipitation. Fig. 1a shows walls being hung above
71 street roofs of a food court, and Fig. 1b displays walls partially covering street roofs of a retail
72 center. Each shop or restaurant has its own enclosed space with air conditioners inside for
73 cooling in summer (April to September) and with doors connected to the semi-open streets.
74 These semi-open outdoor environments are naturally ventilated to reduce energy consumption.
75 Such semi-open street roof designs are used to provide convenience for pedestrians, but they
76 possibly deteriorate UCL ventilation performance. This paper aims to quantitatively evaluate
77 these effects. Although thermal buoyancy force induced by temperature difference and
78 atmospheric stability also influence urban airflows and UCL ventilation [19, 28-29], this paper
79 takes the first step to consider a neutral atmospheric condition assuming that the ambient wind
80 velocity is sufficiently large and thermal effects are negligible.

81 In building ventilation, as reviewed by Chen [27], indoor ventilation indices have been
82 widely used to evaluate how external air enters a room and ventilates it. In recent years,
83 researchers have started to apply similar concepts to estimate UCL ventilation [2,4-11, 24, 28-32,
84 37], including ventilation flow rate and air change rate per hour (ACH) [4, 6-7, 28-30], pollutant
85 exchange rate [31], pollutant retention time and purging flow rate [2,8, 24], age of air and air
86 exchange efficiency [32], city breathability [10-11] etc. This paper emphasizes the quantitative
87 analysis of UCL ventilation induced by rural wind assuming that rural air is relatively clean.
88 Flow rates across street openings and street roofs are first analyzed to quantify the mechanisms
89 of air exchange [37], moreover the local mean age of air [32] is used to quantify how long the
90 external air can reach a place after it enters the UCL. Finally, the UCL purging flow rate [2, 8] is
91 also applied to estimate the net UCL ventilation capacity induced by both mean flows and
92 turbulent diffusions.

93 Tracer gas techniques [27, 44] are usually used to measure indoor ventilation indices.
94 However for both open or semi-open outdoor spaces, ventilation indices such as age of air and
95 purging flow rate are difficult to be measured by tracer gas techniques, since outdoor
96 environment is not an enclosed space with more complicated openings than indoor, moreover
97 perfect mixing and uniform pollutant generation rate in UCLs are difficult to experimentally
98 control. Thus the literatures [5-11, 24, 28-32] usually use experimental data to validate the
99 reliability of CFD methods in predicting concentration and airflow field, then analyze outdoor
100 ventilation indices by using CFD simulations. This paper also utilizes similar methodologies.

101

102 **2. Methodologies**

103 **2.1 Turbulence modeling in CFD simulations**

104 Large eddy simulation (LES) models are known to perform better in predicting turbulent
105 flows than the Reynolds-Averaged Navier-Stokes (RANS) approaches, but the applicability of
106 LES models is more problematic due to its much longer computational time required than RANS
107 approaches and some issues regarding the implementation of wall and inlet boundary conditions
108 [33-34]. Considering that RANS turbulence models are more time-saving and provide reasonable
109 results for mean flows and the spatial average flow properties [33], this paper adopted RANS
110 turbulence models for evaluating UCL ventilation.

111 UCL ventilation relies on both mean flows and turbulence within the UCL [8, 37].
112 According to the literatures [35-36], the modified $k-\varepsilon$ models, for example RNG $k-\varepsilon$ model, are
113 able to correct the drawback of the standard $k-\varepsilon$ model that severely over-predicts turbulent
114 kinetic energy in separated flows around front corners of buildings, however, they fail to predict
115 the sizes of reattachment lengths behind buildings and under-predict the velocity in weak wind
116 regions. It is desirable to compare different RANS turbulence models in predicting urban
117 airflows and UCL ventilation to provide a sensitivity study, including standard $k-\varepsilon$ model, RNG
118 $k-\varepsilon$ model, realizable $k-\varepsilon$ model and Reynolds stress model (RSM).

119

120 **2.2 Experimental and CFD set-ups in the validation case**

121 This paper aims to study UCL ventilation in low-rise idealized and typical urban models
122 consisting of two-storey buildings (about 7m tall). Wind tunnel data was first used to evaluate
123 the reliability of CFD methodologies. As shown in Fig. 2a, Hang et al. [37] performed some

124 wind tunnel experiments to investigate the flow in a small-scale urban model with four square
 125 building blocks (building height $H=0.069\text{m}$, building width $B=3H$) and two crossing streets
 126 (street width $W=H$, urban size $L=7H$). The approaching wind was parallel to the main street and
 127 perpendicular to the secondary streets. The scale ratio between small-scale and full-scale models
 128 is 1:100. Thus in full-scale real conditions $H=W\approx 7\text{m}$, $B=3H\approx 21\text{m}$, $L\approx 49\text{m}$. In small-scale
 129 models the height of 1.5 mm ($0.22H$) corresponds to the face level (1.5 m) in full-scale
 130 conditions.

131 The measurements were performed in the closed-circuit type wind tunnel at the Laboratory
 132 of Ventilation and Air Quality, University of Gävle, Sweden, with the working section of 11m
 133 long, 3m wide, 1.5m tall. Thus the blockage ratio is about 0.6%, which represents the percentage
 134 of the small-scale urban model obstructing the test section area ($3\text{m}\times 1.5\text{m}$) of the wind tunnel.
 135 The stream-wise, lateral and vertical directions are represented by x , y , z . Hotwire anemometer
 136 was used to measure vertical profiles of velocity ($U_m(z)$) and turbulence intensity ($I(z)$) in the
 137 upstream free flow of wind tunnel (see Fig. 2b), horizontal profiles of velocity $\bar{u}(x)$ and
 138 turbulence intensity $I(x)$ along the main street centerline (see Fig. 3b) at $z=0.11H$ (7.5mm). The
 139 sampling frequency was 100 Hz. The measurement time was 30s for each point. It is worth
 140 mentioning that, the hotwire is only sensitive to velocity components perpendicular to it (i.e. the
 141 vertical velocity \bar{w} and the stream-wise velocity \bar{u}). So data measured by the hotwire were
 142 actually $\sqrt{\bar{u}^2 + \bar{w}^2}$. Here the hotwire was only located where the span-wise (y) velocity \bar{v} was
 143 zero, including in the upstream free flow and along the main street centerline, so the measured
 144 data were actually the velocity magnitude ($U=\sqrt{\bar{u}^2 + \bar{v}^2 + \bar{w}^2}$).

145 Because there were no roughness elements in wind tunnel experiments, a thin neutral
 146 atmospheric boundary layer (ABL) and a sharp vertical profile of velocity was produced in the
 147 upstream free flow (see Fig. 2b). We only used the measured profiles ($U_m(z)$ and $I(z)$) in Fig. 2b
 148 to provide boundary conditions at domain inlet in the CFD validation case. At domain inlet,
 149 turbulent kinetic energy is defined as $k(z)=1.5(I U_m)^2$ and its dissipation rate is $\varepsilon(z)=C_\mu^{3/4}k^{3/2}/l$,
 150 where $C_\mu=0.09$ and l is the turbulent characteristic length scale. Note that, the maximum velocity
 151 in the upstream free flow of wind tunnel experiments was 13.33 m/s, however in cases for
 152 ventilation analysis, we used a realistic approaching wind (see Eq. (1a)) with a spatial mean
 153 velocity of about 3.2 m/s, so in the validation case we actually utilized a smaller fitting velocity

154 profile (maximum velocity is 3.24 m/s, see Fig. 2b) with the same thickness of ABL as that in
 155 wind tunnel and the similar spatial mean velocity (about 3.2m/s) as that in Eq. (1a). According to
 156 Snyder [39], Reynolds-number independence can be satisfied if the Reynolds number is greater
 157 than 4000, i.e. the main structure of turbulence can be almost entirely responsible for the bulk
 158 transport of momentum and heat or mass transfer. If the velocity $z=H=0.069\text{m}$ in the upstream
 159 free flow (see Fig. 2b) is defined as the reference velocity $U_{\text{ref}} \approx 2.94\text{m/s}$, the reference Reynolds
 160 number ($Re_H = \rho U_{\text{ref}} H / \mu \approx 13887$) is much larger than 4000, Thus the technique of using a smaller
 161 inflow velocity (i.e. 3.24m/s) can ensure Reynolds number independence.

162 The CFD code FLUENT 6.3 [38] was used to solve the steady-state isothermal turbulent
 163 flows. For CFD simulations, we used the same small-scale urban geometries ($H=0.069\text{m}$) as
 164 those in wind tunnel experiments. Only half computational domain was used to reduce the
 165 calculation time. Fig. 3a displays the computational domain and boundary conditions in the CFD
 166 validation case. The computational domain is $14.5H$ wide (1 m) in the lateral (y) direction and
 167 $11H$ tall (0.75 m) in the vertical (z) direction. Thus the blockage ratio is about 1.9% (less than
 168 3%) satisfying the requirement of the literature [40]. No-slip wall boundary condition was
 169 utilized at wall surfaces, and zero normal gradient boundary condition was used at domain
 170 outlet, domain roof, domain lateral boundary, domain symmetry boundary.

171 Fig. 3b displays the grid arrangements in x - y plane of the validation case. Finer grids are
 172 produced within the UCL and near wall surfaces, building corners, street openings. The grid size
 173 near the ground is $0.036H$ ($dz=2.5\text{mm}$). There are 6 cells vertically from $z=0$ to the pedestrian
 174 height ($z=20\text{mm}=0.29H$). The grid size near building roofs at $z=H$ is $0.022H$ ($dz=1.5\text{mm}$). The
 175 horizontal grid size (dx and dy) near building surfaces varies from $0.022H$ to $0.043H$. The
 176 maximum expansion ratio from building surfaces to the surrounding is 1.15 and the total
 177 number of hexahedral cells is about 0.82 million.

178 In the CFD validation case, all CFD set-ups including computational domain size,
 179 boundary conditions and grid arrangements fulfilled the major CFD guidelines recommended by
 180 Tominaga et al. [40].

181

182 **2.3 CFD set-ups for flow modelling**

183 After the CFD validation case, more urban configurations with or without semi-open street
 184 roofs and various ambient wind directions were investigated. To better illustrate idealized urban

185 models, all test cases were defined as Case [number of rows-number of columns, wind direction,
 186 roof type]. 'Open' roof type denotes open street roofs; As shown in Fig. 4a-4c, four wind
 187 directions of 0° , 15° , 30° , 45° were included. So the name of validation case is Case [2-2, 0,
 188 Open] with four buildings (2 rows, 2 columns), a parallel approaching wind (0°) and open street
 189 roof ('Open' roof type). As displayed in Fig. 4c, a bigger urban model with 16 buildings (4
 190 columns, 4 rows, urban size $L=15H \approx 105\text{m}$ in full scale) was also investigated in CFD
 191 simulations. Besides the 'Open' roof type, Fig. 5 shows the other five types studied in CFD
 192 simulations. 'Fully-covered' roof type (see Fig. 5a) means walls entirely covering street roofs
 193 with a coverage ratio(λ_a) of 100% at $z=H$, and 'Partly-covered' roof type (see Fig. 5b) represents
 194 street roofs being partly covered ($\lambda_a=80\%$) by walls at $z=H$. Roof types of 'Hung1.5H',
 195 'Hung1.2H' and 'Hung1.1H' (see Fig. 5c) represent walls being hung above street roofs ($\lambda_a=100\%$)
 196 at $z=1.5H$, $1.2H$ and $1.1H$, respectively. As summarized in Table 1, total 48 test cases were
 197 numerically investigated.

198 For test cases with a parallel approaching wind (0°), the computational domain and
 199 boundary conditions were similar as the CFD validation case. A power-law velocity profile was
 200 applied at domain inlet with a power-law exponent of 0.16(see Eq. (1a)). As reported by Lien
 201 and Yee [41], it represents a neutral atmospheric boundary layer (ABL) with a depth of 1.8 m
 202 created in the wind tunnel by using spires and floor roughness with a roughness length of
 203 approximately $z_0=0.001$ m. In full-scale real conditions, it corresponds to a neutrally-stratified
 204 ABL with a surface roughness of $z_0=0.1\text{m}$ [42] (i.e. a neutral ABL above open rural area with a
 205 regular cover of low crop and occasional large obstacles [43]) The spatial mean velocity at
 206 domain inlet calculated from Eq. (1a) approximately equals to that calculated from the inflow
 207 velocity profile of the CFD validation case (see Fig. 2b).The inlet profiles of turbulent kinetic
 208 energy and its dissipation rate were calculated by Eq. (1b)-(1c)) [30,41].

$$209 \quad \bar{u}(z) = U_0(z) = U_H (z/H)^{0.16}, \bar{v}(z) = \bar{w}(z) = 0 \quad (1a)$$

$$210 \quad k_0(z) = u_*^2 / \sqrt{C_\mu} \quad (1b)$$

$$211 \quad \varepsilon_0(z) = C_\mu^{3/4} k_0(z)^{3/2} / (\kappa_v z) \quad (1c)$$

212 where the friction velocity $u_* = 0.24 \text{ ms}^{-1}$, $\kappa_v = 0.41$ is von Karman's constant, $U_H = 2.66 \text{ ms}^{-1}$ is the
 213 reference velocity at $z=H=0.069\text{m}$ of domain inlet.

214 For test cases with a non-parallel approaching wind (15° , 30° , 45°), there are two domain
 215 inlets and two domain outlets(see Fig. 4a). At domain inlets, the power-law velocity profiles
 216 (stream-wise velocity $\bar{u} = U_0(z)\cos\theta$, span-wise velocity $\bar{v} = U_0(z)\sin\theta$ and vertical velocity
 217 $\bar{w}(z) = 0$) and profiles of turbulent quantities in Eq. (1b)-(1c) were used to provide boundary
 218 conditions. Zero normal gradient conditions were still used at two domain outlets and domain
 219 roof.

220 Fig. 6a and 6b show two examples of the grid arrangements in test cases with four (2×2)
 221 buildings and semi-open street roofs. Note that, the thickness of hung walls to produce semi-
 222 open street roofs was zero in CFD models. The grid arrangements were similar with those in the
 223 CFD validation case except three points: The first is that the grids near semi-open street roofs
 224 (i.e. at $z=1.1H$, $1.2H$, $1.5H$) are also fine with a grid size of $dz=0.014H=1\text{mm}$ (see Fig. 6b); The
 225 second is that for test cases with 16 buildings the maximum expansion ratio of grid size from
 226 wall surfaces to the surrounding is 1.2 which is less than 1.3 and satisfies the CFD guideline
 227 [40];The third is that the grid number in cases with 'Partly-covered' roof type (see Fig. 6a) is a
 228 little more than the other roof types, because fine grids with grid size of $dy=0.029H$ were also
 229 generated near lateral boundaries of partly-covered street roofs. The maximum grid number is
 230 about 3.5 million in Case [4-4,45, Partly-covered].

231 All transport equations were discretized by the second order upwind scheme to increase the
 232 accuracy and reduce numerical diffusion. The SIMPLE scheme was used for the pressure and
 233 velocity coupling. CFD simulations were run until all residuals became constant. Overall,
 234 residual for the continuity equation was below 10^{-4} , residuals for the velocity components and k
 235 were below 10^{-7} , residuals for pollutant concentration and ε were below 0.5×10^{-5} and 0.5×10^{-4}
 236 respectively.

237

238 **2.4 Ventilation assessment indices**

239 **2.4.1 Age of air**

240 The local mean age of air (τ_p) was originally defined in indoor ventilation and can be
 241 measured by tracer gas techniques [44]. The local age of air in UCLs represents the mean time
 242 required for the external young air to reach a point since it enters UCLs. If the age of air in rural
 243 areas is zero, the greater age of air in UCLs represents a greater probability to be polluted. The

244 UCL age of air depicts how rural air is supplied and distributed within UCLs. Hang et al. [32]
 245 first introduced the homogeneous emission method [44] to numerically predict age of air in
 246 UCLs.

247 The governing equations of time-averaged pollutant concentration (\bar{c} , kg/m³) and the age of
 248 air (τ_p , s) are displayed as below:

$$249 \quad \bar{u}_j \frac{\partial \tau_p}{\partial x_j} - \frac{\partial}{\partial x_k} (K_c \frac{\partial \tau_p}{\partial x_k}) = 1 \quad (2)$$

$$250 \quad \bar{u}_j \frac{\partial \bar{c}}{\partial x_j} - \frac{\partial}{\partial x_j} (K_c \frac{\partial \bar{c}}{\partial x_j}) = S_c \quad (3)$$

251 where \bar{u}_j is the velocity components ($\bar{u}, \bar{v}, \bar{w}$) in the stream-wise (x), span-wise (y) and
 252 vertical (z) directions, $K_c = \nu_t / S_{ct}$ is the turbulent eddy diffusivity of pollutants, ν_t is the
 253 kinematic eddy viscosity, S_{ct} is the turbulent Schmidt number ($S_{ct}=0.7$) [8, 10, 20, 45]. S_c is the
 254 pollutant source term (kgm⁻³s⁻¹).

255 In the homogeneous emission method[44], a relation between these two variables was
 256 mathematically derived. If a homogenous pollutant release rate (S_c , kgm⁻³s⁻¹) is defined in the
 257 entire UCL, the age of air (τ_p , s) can be calculated:

$$258 \quad \tau_p = \bar{c} / S_c \quad (4)$$

259 Eq. (4) illustrates a relationship that, with a uniform pollutant source in the entire UCL,
 260 higher pollutant concentration at a point represents that it takes the external clean air a longer
 261 time to arrive.

262 Fig.6c shows an example of defining uniform pollutant source in the entire UCL. In this
 263 paper, the pollutant emission rate was small ($S_c=10^{-7}$ kg m⁻³s⁻¹) to ensure the source release
 264 producing little disturbance to the flow field. The inflow concentration at domain inlet was
 265 defined zero, and the zero normal flux condition was used at wall surfaces. At all other
 266 boundaries zero normal gradient condition was utilized.

267 Because the age of air in small-scale urban models is small (scale ratio 1:100), the age of air
 268 was normalized in Eq. (5a). To compare the age of air in the entire UCLs, this paper also
 269 analyzed the normalized spatial mean age of air ($\langle \tau_p^* \rangle$) in Eq. (5b)

$$270 \quad \tau_p^* = \tau_p \times 100 \quad (5a)$$

$$271 \quad \langle \tau_p^* \rangle = \int_{Vol} \tau_p^* dx dy dz / Vol \quad (5b)$$

272 where Vol is the entire UCL volume.

273

274 2.4.2 Ventilation flow rates and UCL purging flow rates

275 Both mean flows and turbulent diffusions are significant factors for UCL ventilation [37]
 276 and pollutant removal [8]. The purging flow rate represents the net flow rate induced by both
 277 mean flows and turbulent diffusions for a volume to be purged out by wind through it. It has
 278 been used to quantify the ventilation in UCLs [2] and at the pedestrian levels [8].

279 This paper mainly emphasizes the purging flow rate for the entire UCL. If a passive
 280 contaminant source is generated within the entire UCL (see Fig. 6c) with a uniform emission rate
 281 (here $S_c = 10^{-7} \text{ kg m}^{-3} \text{ s}^{-1}$), the UCL purging flow rate ($PFR, \text{ m}^3/\text{s}$) is calculated in Eq. (6).

$$282 \quad PFR = \frac{S_c \times Vol}{\langle \bar{c} \rangle} = \frac{S_c \times Vol}{\int_{Vol} \bar{c} dx dy dz / Vol} \quad (6)$$

283 Here $\langle \bar{c} \rangle$ is the spatially-averaged concentration in the entire UCL volume (Vol). It is
 284 worth mentioning that PFR is independent of pollutant sources, and illustrates the net UCL
 285 ventilation capacity due to both mean flows and turbulent diffusion.

286 Because PFR is small for small-scale urban models (scale ratio 1:100), PFR is normalized
 287 by the reference flow rate (Q_∞).

$$288 \quad PFR^* = \frac{S_c \times Vol}{\langle \bar{c} \rangle Q_\infty} = \frac{PFR}{Q_\infty} \quad (7)$$

$$289 \quad Q_\infty = H \times \int_0^H U_0(z) dz \quad (8)$$

290 where $Q_\infty = 0.01093 \text{ m}^3/\text{s}$ is the flow rate far upstream through the same area with a windward
 291 street opening (area $A = H \times H$), $U_0(z)$ is defined in Eq. (1a).

292 Fig. 4b-4c show the definition of street openings in test cases with 4 (2×2) and 16 (4×4)
 293 buildings. To quantify the ventilation pattern, all flow rates entering and leaving UCL volumes
 294 were normalized by the reference flow rate (Q_∞), including Q^* due to mean flows (see Eq. (9))
 295 and $Q_{\text{roof}}^*(\text{turb})$ due to turbulence fluctuations across street roofs [37] (see Eq. (10)):

$$296 \quad Q^* = \int_A \vec{V} \cdot \vec{n} dA / Q_\infty \quad (9)$$

$$297 \quad Q^*_{roof} (turb) = \pm \int 0.5 \sigma_w dA / Q_\infty \quad (10)$$

298 where in Eq.(9), \vec{V} is velocity vector, \vec{n} is the normal direction of street openings or street roofs, A is
 299 surface area; In Eq.(10), $\sigma_w = \sqrt{w'w'} = \sqrt{2k/3}$ is the fluctuation velocity on street roofs based on
 300 the approximation of isotropic turbulence (k is the turbulent kinetic energy).

301 Due to the flow balance by mean flows, the total flow rate leaving UCL (Q_{out}) through
 302 UCL boundaries equals to that entering UCL (Q_{in}). They are named as the total flow rates by
 303 mean flows Q_T and are normalized by the reference flow rate Q_∞ .

$$304 \quad Q_T^* = Q_{in}^* = Q_{out}^* \quad (11)$$

305 By applying the above concepts, this paper quantifies the effects of semi-open street roofs
 306 and various wind directions on the age distribution, the ventilation pattern and the entire UCL
 307 ventilation capacity.

308

309 3. Results and discussions

310 3.1 Evaluation and validation of CFD results

311 Fig. 7 shows the validation of CFD results by using the measured horizontal profiles of
 312 velocity and turbulent intensity along street centerline at $z=0.11H$ in Case [2-2.0, Open]. $x/H=0$
 313 denotes the location of windward street opening (at O1). The velocity was normalized by the
 314 inflow velocity at domain inlet at the same height ($z=0.11H$). In comparison to wind tunnel data,
 315 the standard $k-\varepsilon$ model and realizable $k-\varepsilon$ model predicted the velocity profile better than RNG $k-$
 316 ε model and RSM model. More importantly the standard $k-\varepsilon$ model performed the best in
 317 predicting airflow velocity in the downstream region of the main street. This finding agrees with
 318 the literature [35-36] that non-standard $k-\varepsilon$ models perform better in predicting separate flows
 319 but do worse in predicting airflow velocity in weak wind regions. All RANS turbulence models
 320 can only predict the shape of turbulence intensity profile, thus $Q^*_{roof}(turb)$ calculated by CFD
 321 simulations were only used to provide a reference study and the relative values of $Q^*_{roof}(turb)$
 322 among different test cases were emphasized. Since the better prediction of mean flows within

323 UCL and along the streets is more important, this paper hereby regards the standard $k-\varepsilon$ model
 324 as the default turbulence model in the following CFD simulations.

325 For the validation case (medium grid, 0.8 million), a finer grid arrangement with the
 326 minimum grid size of $0.014H$ and grid number of 1.3 million was used to perform a grid
 327 independence study. As displayed in Fig. 7c, numerical results were not sensitive to the grid
 328 refinement, indicating present grid arrangements in Fig. 3b were sufficiently fine.

330 3.2 Ventilation assessment in cases with four buildings

331 In this subsection, the effects of semi-open street roofs and various wind directions in test
 332 cases with four buildings and two crossing streets (i.e. Case [2-2, wind direction, roof type], see
 333 Table 1) were investigated.

335 3.2.1 Effect of semi-open street roofs in four example test cases

336 Fig. 8a displays three-dimensional (3D) streamline in four test cases (only half domain, 0°),
 337 i.e. Case [2-2, 0, Open], Case [2-2, 0, Hung1.2H], Case [2-2, 0, Partly-covered], Case [2-2,
 338 0, Fully-covered]. Channel flows are found in the main streets parallel to the approaching wind
 339 and 3D helical flows exist in the secondary streets. These channel and helical flows produce air
 340 exchange and turbulent diffusion through street openings and street roofs. Different semi-open
 341 street roofs may produce various flow pattern and ventilation capacity but this effect cannot be
 342 clearly displayed by only 3D streamlines in Fig. 8a. To quantify this effect, Fig. 8b shows the
 343 normalized age of air ($\tau_p^* = \tau_p \times 100$) in $z=0.22H$ (i.e. 1.5m in full scale) and normalized flow
 344 rates (Q^*) in these four test cases. Positive values denote air entering UCLs and negative ones
 345 represent air leaving UCLs. τ_p^* along the main street (Street 1 and Street 3) is relatively small
 346 (i.e. air is relatively young) because Q^* through O1 and O3 are always large ($Q^*(O1)=1.048$ to
 347 0.848 ; $Q^*(O3)=-0.551$ to -0.813). In the secondary streets (Street 2 and Street 4), Q^* through O2
 348 (O4) are small (only 0.086 to -0.019). Thus the roof ventilations are more significant to the
 349 secondary streets. For example, in Case [2-2, 0, Open], τ_p^* in Street 2 (or Street 4) is similar
 350 with that in Street 3 because the flow rates across street roofs are comparable to those across O1
 351 and O3, including the upward and downward flow rates due to mean flows ($Q_{\text{roof}}^*(\text{out})=-0.825$
 352 and $Q_{\text{roof}}^*(\text{in})=0.148$), and the effective flow rate induced by turbulence fluctuations

353 ($Q^*_{\text{roof(turb)}}= 1.211$). For types of 'Hung1.2H' and 'Partly-covered', roof ventilation capacity
 354 significantly decreases, including $Q^*_{\text{roof(out)}}=-0.825$ to -0.424 and -0.306 , $Q^*_{\text{roof(in)}}=0.148$ to
 355 0.116 and 0.008 , $Q^*_{\text{roof(turb)}}=1.211$ to 1.059 and 0.258 . Moreover Q^* across O1 decreases a little
 356 (1.048 to 0.999 and 0.950) due to the displacement by semi-open street roofs, and Q^* across O3
 357 increases a little (-0.551 to -0.684 and -0.685). These results show that semi-open street roofs not
 358 only pose additional flow resistances and therefore reduce the ventilation by vertical mean flows
 359 and turbulence across street roofs, but also influence the inflow rates and redistribution of
 360 airflows along the streets within UCL, especially driving more air across Street 3 (O3). Thus in
 361 contrast to Case [2-2, 0, Open], models with semi-open street roofs obtain much greater τ_p^* and
 362 older air in the secondary streets due to the weakened roof ventilation. An extreme example is
 363 'Fully-covered' type, in which the flow rates across street roofs are zero, and τ_p^* in the
 364 secondary street (125 to 225) is much greater than that in the main street (0-45). The UCL spatial
 365 mean age of air $\langle \tau_p^* \rangle$ with 'Open' and 'Hung1.2H' types are 24.3 and 37.7, which is much
 366 smaller than $\langle \tau_p^* \rangle$ with 'Partly-covered' and 'Fully-covered' types (54.9 and 90.4), confirming
 367 that the 'Hung1.2H' type provide better overall UCL ventilation than 'Partly-covered' and 'Fully-
 368 covered' types.

369

370 3.2.2 Effect of ambient wind directions in four example test cases

371 Fig. 9 displays 3D streamline, τ_p^* and Q^* in Case [2-2, 0, Hung1.5H], Case [2-2, 15,
 372 Hung1.5H], Case [2-2, 30, Hung1.5H] and Case [2-2, 45, Hung1.5H]. The flow patterns are
 373 obviously different and flow rates are redistributed. With a parallel approaching wind, air enters
 374 UCL through O1, O2 and O4, then leaves through O3. Moreover 3D helical flows mainly exist
 375 in Street 2 and Street 4 where air is relatively old. With non-parallel approaching wind, air enters
 376 UCLs across O1 and O2, then leaves through O3 and O4; Recirculation flows exist in all four
 377 streets and τ_p^* is relatively large in the downstream streets (Street 3 and Street 4) and in
 378 recirculation regions. If wind directions change from 0° to 15° , 30° , 45° , both roof ventilation and
 379 overall UCL ventilation are improved including $Q^*_{\text{roof(out)}}$ varies from -0.547 (0°) to -0.939 (15°),
 380 -0.919 (30°) and -0.730 (45°), $Q^*_{\text{roof(in)}}$ changes from 0.106 (0°) to 0.586 (15°), 1.092 (30°) and
 381 1.041 (45°), and $\langle \tau_p^* \rangle$ decreases from 29.6 (0°) to 22.6 (15°), 18.9 (30°) and 18.5 (45°).
 382 These results confirm that 30° and 45° produce better UCL ventilation than 0° and 15° .

383 As discussed and reported by the literature [2, 8-11, 18-20, 24, 31-32, 45], turbulent Schmidt
 384 numbers (S_{ct}) may influence numerical results of pollutant dispersion. As displayed in Table 2,
 385 the effects of different S_{ct} and turbulence models are studied in Case [2-2, 0, Open] to quantify
 386 the sensitivity of turbulence models and S_{ct} on UCL ventilation: $S_{ct}=1.0, 0.7$ and 0.4 are used in
 387 standard $k-\varepsilon$ model, $S_{ct}=0.7$ in RNG $k-\varepsilon$ model, and $S_{ct}=0.7$ in Realizable $k-\varepsilon$ model. With the
 388 same standard $k-\varepsilon$ model and S_{ct} of $1.0, 0.7$ or 0.4 , $\langle \tau_p^* \rangle$ in the entire UCL are $26.4, 24.3$ and
 389 21.2 , respectively, showing that smaller S_{ct} may enhance pollutant dispersion by turbulent
 390 diffusion and slightly reduce the age of air. With the same S_{ct} of 0.7 , realizable $k-\varepsilon$ model and
 391 RNG $k-\varepsilon$ model obtain different flow rates through O3 and street roofs which result in a little
 392 greater $\langle \tau_p^* \rangle$ (27.2 and 28.2) than that by standard $k-\varepsilon$ model (24.3). Especially Q^* across O3
 393 predicted by RNG $k-\varepsilon$ model is much smaller than those by the other two, which can be
 394 explained by the fact that RNG $k-\varepsilon$ model significantly over-predicts $Q^*_{\text{roof(out)}}$ (-1.127) than the
 395 other two (-0.825 and -0.844). To be consistent, standard $k-\varepsilon$ model with S_{ct} of 0.7 was selected
 396 as the default settings in CFD simulations.

397

398 3.2.2 Overall ventilation assessment in cases with four (2×2) buildings

399 To quantify the effect of semi-open street roofs on UCL ventilation flow rates, Fig. 10
 400 shows Q^* through O1-O4 and $Q^*_{\text{roof(out)}}$, $Q^*_{\text{roof(in)}}$, $Q^*_{\text{roof(turb)}}$ in all test cases with 4 buildings
 401 and wind directions of 0° to 45° . Roof types change from 'Open', 'Hung1.5H', 'Hung1.2H',
 402 'Hung1.1H', to 'Partly-covered' and 'Fully-covered' (reading figure from left to right). Roof
 403 ventilations for 'Fully-covered' type are all zero. For wind directions of 0° and 15° (see Fig.10a-
 404 10b), roof type variations result in a slightly decreasing flow rates across O1 and an increasing
 405 flow rates across O3. More importantly, the flow rates across street roofs are all significantly
 406 weakened, including $Q^*_{\text{roof(out)}}$ from -0.825 (0°) and -1.156 (15°) to 0 , $Q^*_{\text{roof(in)}}$ from 0.148 (0°)
 407 and 0.619 (15°) to 0 , and $Q^*_{\text{roof(turb)}}$ from 1.211 (0°) and 1.315 (15°) to 0 . Moreover, Q^* across
 408 O2 and O4 are relatively small for wind direction of 0° (see Fig. 10a), but they become
 409 considerably large for wind direction of 15° (see Fig. 10b). For wind directions of 30° and 45°
 410 (see Fig.10c-10d), similar findings exist due to such roof type variations that all roof ventilation
 411 indices decrease quickly and Q^* across street openings decrease a little.

412 To quantify the reduction of UCL ventilation as roof types varying from 'Open' type to
 413 'Fully-covered' type, the normalized ventilation ratio (*NVR*) is defined as the value of ventilation
 414 indices in a case divided by those with 'open street roofs' and the same wind direction. Thus for
 415 cases with open street roofs, $NVR=1$, and Q^* across street roofs for 'Fully-covered' roof type are
 416 all zero ($NVR=0$). Fig. 11 displays $Q^*_{\text{roof}}(\text{in})$ and $Q^*_{\text{roof}}(\text{out})$, $Q^*_{\text{roof}}(\text{turb})$, total normalized flow
 417 rates by mean flows (Q_T^*), normalized UCL purging flow rate (PFR^*), $\langle \tau_p^* \rangle$ in the entire
 418 UCL, and their *NVR* values for all 24 cases with 4 buildings. With the same roof type, wind
 419 direction of 30° and 45° obtain greater $Q^*_{\text{roof}}(\text{in})$ and $Q^*_{\text{roof}}(\text{turb})$, larger Q_T^* and PFR^* , smaller
 420 $\langle \tau_p^* \rangle$, showing that 30° and 45° produce better UCL ventilation than 0° and 15° . In addition,
 421 Fig. 11a-11b also confirm that, all roof ventilation indices decrease as roof type varies from
 422 'Open' to 'Partly-covered', and *NVR* for 'Partly-covered' type are as small as 5.6% to 34% for
 423 $Q^*_{\text{roof}}(\text{in})$, 18.0%-37.1% for $Q^*_{\text{roof}}(\text{out})$, and 21.3%-22.6% for $Q^*_{\text{roof}}(\text{turb})$ respectively. Fig.
 424 11c-11d displays that overall UCL ventilation basically decreases from 'Open' type to 'Fully-
 425 covered' type, indicated by the fact as below: the *NVR* of Q_T^* are 87%-99% for 'Hung1.5H' type,
 426 81%-92% for 'Hung1.2H' type, 67%-78% for 'Hung1.1H' type, 57%-72% for 'Partly-covered'
 427 type and 41%-62% for 'Fully-covered' type; the *NVR* of PFR^* are from 82%-110%, 64%-110%,
 428 52%-104% to 44%-87% and 27%-64%, and the *NVR* of $\langle \tau_p^* \rangle$ are from 90%-122%, 91%-
 429 155%, 96%-190% to 115%-226% and 156-373%. Overall, Fig. 11d-11e confirm that roof types
 430 of 'Hung1.5H', 'Hung1.2H' and 'Hung1.1H' may produce relatively considerable UCL ventilation
 431 in contrast to 'Open' type (i.e. *NVR* are 52%-110% for PFR^* and 91%-190% for $\langle \tau_p^* \rangle$).
 432 Considering 'Hung1.1H' and 'Hung1.2H' types are more realistic, they are proposed as better
 433 semi-open street roof configurations. Meanwhile, Fig. 11d-11e also verify that, if roof types
 434 change from 'Open' to 'Fully-covered', overall UCL ventilation with 0° wind direction may
 435 decrease much more significantly (*NVR* are 100% to 27% for PFR^* , and 100% to 372% for
 436 $\langle \tau_p^* \rangle$) than the other wind directions, because the secondary streets with 0° wind direction and
 437 semi-open street roofs tend to be poorly ventilated.

438

439 3.3 Ventilation assessment in test cases with sixteen buildings

440 What happen if urban size enlarges? To quantify this effect, test cases with 16 buildings are
 441 investigated, as summarized in Table 1. Fig. 12 displays normalized age of air in four test cases,

442 i.e. Case [4-4, 0, Hung1.2H], Case [4-4, 15, Hung1.2H], Case [4-4, 30, Hung1.2H], Case [4-4, 45,
 443 Hung1.2H]. The ventilation patterns are similar with those consisting of 4 buildings. For wind
 444 direction of 0° , air mainly enters UCL across windward street openings of O1a, O1b, O1c, and
 445 leaves UCL through leeward openings of O3a, O3b, O3c. For wind directions of 15° , 30° , and
 446 45° , air enters UCL through O1a to O1c and O2a to O2c, then leaves UCL across O2a to O2c
 447 and O4a to O4c. Age of air is relatively large and air is old in recirculation regions and
 448 downstream regions.

449 UCL ventilation indices and their normalized ventilation ratios (*NVR*) in all 24 test cases
 450 with 16 buildings are quantitatively analyzed, including Q_{roof}^* (in) and Q_{roof}^* (out) in Fig. 13a,
 451 Q_{roof}^* (turb) in Fig. 13b, Q_T^* in Fig. 13c, *PFR** in Fig. 13d and $\langle \tau_p^* \rangle$ in the entire UCL in Fig.
 452 13e. It is found that UCL ventilation indices basically become a little better if wind directions
 453 change from 0° and 15° to 30° and 45° . More importantly, roof type variations from 'Open' to
 454 'Fully-covered' produce a large decreasing rate of overall UCL ventilation and obtain
 455 macroscopically older air, which can be represented by the below data. For roof ventilation
 456 indices(see Fig. 13a-13b), *NVR* for 'Fully-covered' type are all zero, and those for 'Partly-
 457 covered' type are 11%-23% for Q_{roof}^* (in), 28%-39% for Q_{roof}^* (out), and 16%-22% for Q_{roof}^*
 458 (turb). For overall UCL ventilation, *NVR* of Q_T^* (see Fig. 13c) are 81%-96% for 'Hung1.5H' type,
 459 78%-87% for 'Hung1.2H' type, 65%-86% for 'Hung1.1H' type, 52%-61% for 'Partly-covered'
 460 type and 28%-50% for 'Fully-covered' type, and *NVR* of *PFR**(see Fig. 13d) for the above roof
 461 types are 84%-90%, 76%-87%, 65%-86%, 52%-68%, and 36%-45% respectively, moreover *NVR*
 462 of $\langle \tau_p^* \rangle$ increase from 111%-120%, 115%-131%, 116%-154% to 148%-192%, 223%-279%
 463 (i.e. air becomes older). Results also confirm that, 'Hung1.5H', 'Hung1.2H' and 'Hung1.1H' types
 464 produce a little smaller but comparable UCL ventilation in contrast to 'Open' type. Thus for cases
 465 with 16 buildings, the roof types of 'Hung1.2H' and 'Hung1.1H' are better choices considering
 466 they are more realistic designs.

467

468 3.4 Effect of urban size on UCL ventilation

469 To quantify how overall UCL ventilations change if building number or urban size
 470 increases, Fig. 13b-13e also compares Q_{roof}^* (turb), Q_T^* , *PFR** and $\langle \tau_p^* \rangle$ between urban
 471 models with 4 or 16 buildings (the smaller or bigger model). By analyzing Fig. 13b-13d, Q_{roof}^*

472 (turb), Q_T^* and PFR^* in the bigger model are found several times (about 3.2-4.7 for Q_{roof}^* , 1.2-
 473 2.6 for Q_T^* , 0.8-3.5 for PFR^*) larger than those in the smaller model. Larger urban model
 474 obtains greater ventilation capacity because their total area of street openings and street roofs are
 475 2 and 5.2 times greater than the smaller one. However it does not represent larger urban model
 476 can produces better overall UCL ventilation. It can be confirmed by Fig. 13e that $\langle \tau_p^* \rangle$ in the
 477 bigger model is about 1.4 to 3.5 times as great as that in the smaller model, showing that the
 478 bigger model obtains macroscopically older air. It is because the bigger model has a UCL
 479 volume of 5.2 times larger than that in the smaller model and requires longer time for wind to
 480 flow through.

481

482 **3.5 Discussions and Future outlooks**

483 Further investigations are still required before formulating a practical guidelines for these
 484 semi-open street roof designs, such as the effect of the surrounding building height, the effect of
 485 atmospheric thermal stratification (not neutral) and buoyancy force due to solar shading, the
 486 analysis of rain-cover and shading capability etc. This paper is one of the first attempts to
 487 quantify and address a relationship between semi-open street roof configurations and UCL
 488 ventilation indices. The methodologies and techniques utilized in this paper are promising, and
 489 possibly provide a valid tool to investigate UCL ventilation in other types of idealized or realistic
 490 urban configurations.

491

492 **4. Conclusions**

493 The arrangements of semi-open street roofs in urban space are effective to protect
 494 pedestrians from strong sunshine and heavy rains or snows. Their effects on urban canopy layer
 495 (UCL) ventilation are still not fully understood. This paper numerically quantified how five types
 496 of semi-open street roofs influence isothermal turbulent airflows and UCL ventilation
 497 performance under a neutral atmospheric condition with various ambient wind directions ($0^\circ, 15^\circ,$
 498 $30^\circ, 45^\circ$). Two small-scale idealized urban models were investigated consisting of 4 (2×2) or 16
 499 (4×4) buildings with uniform building height of $H=0.069\text{m}$, and street aspect ratio of $H/W=1$,
 500 corresponding to full-scale urban models of about 7m tall, 49m and 105m long as the scale ratio
 501 is 1:100. In contrast to 'Open' roof type (open street roof), five kinds of semi-open street roofs
 502 were included: Walls are hung above open street roofs (coverage ratio $\lambda_a=100\%$) at $z=1.1H, 1.2H,$

503 1.5H, i.e. types of 'Hung1.1H', 'Hung1.2H', 'Hung1.5H'; Walls partly cover street roofs at $z=H$
 504 ($\lambda_a=80\%$), i.e. 'Partly-covered' type; Walls are set up to cover the entire street roof at $z=H$
 505 ($\lambda_a=100\%$), i.e. 'Fully-covered' type. The age of air and its spatial mean value, flow rates across
 506 street openings and street roofs, the UCL purging flow rate were numerically analyzed to
 507 quantify UCL ventilation.

508 Results show that the prediction of airflow velocity by using standard $k-\varepsilon$ model agreed
 509 better with wind tunnel data than other three RANS turbulence models. Semi-open street roofs
 510 significantly influence UCL ventilation patterns and redistribute flow rates across street openings
 511 and street roofs. As roof types vary from 'Open' to 'Hung1.5H', 'Hung1.2H', 'Hung1.1H' then to
 512 'Partly-covered' and 'Fully-covered', both roof ventilation and overall UCL ventilation
 513 performance are basically weakened. The net UCL ventilation is the worst for the 'Fully-covered'
 514 type, followed by the 'Partly-covered' type. The roof types of 'Hung1.2H' and 'Hung1.1H' are
 515 proposed because they produce comparable UCL ventilation, meanwhile are more realistic roof
 516 designs. Oblique ambient wind directions of 30° and 45° obtain better UCL ventilation than 15°
 517 and 0° . If the building number increases from 4 (2×2) to 16 (4×4), air in the entire UCL becomes
 518 macroscopically older because the greater UCL volume requires longer time for rural wind to
 519 flow through.

520

521 Acknowledgements

522 This study was financially supported by the National Natural Science Foundation of China
 523 (No. 51108102) and Guangdong Natural Science Foundation (Code S2011040004149). The two
 524 anonymous reviewers who provided constructive suggestions and comments are also gratefully
 525 acknowledged.

526

527 Nomenclature

528	A	area of a surface (m^2)
529	B, H, L, W	building width, building height, total length, street width
530	$\bar{c}, \langle \bar{c} \rangle$	time-averaged pollutant concentration (kgm^{-3}) and its spatial mean value
531	K_c, ν_t	turbulent eddy diffusivity of pollutant and momentum $K_c = \nu_t / S_{ct}$
532	k, ε	turbulent kinetic energy and its dissipation rate

533	\vec{n}	normal direction of street openings or canopy roofs
534	NVR	normalized ventilation ratio in contrast to models with 'open' street roofs
535	PFR, PFR^*	purging flow rate and its normalized value ($PFR^*=PFR/Q_\infty$)
536	Q^*	normalized flow rate through street openings or street roofs
537	Q_{in}^*, Q_{out}^*	normalized total inflow and outflow rate for entire UCL
538	Q_T^*	total ventilation flow rate by mean flows (m^3s^{-1})
539	Q_∞	reference flow rate in upstream free flow to normalize flow rates
540	$Q_{roof}^* (turb)$	normalized effective flow rate across street roofs by turbulence
541	$Q_{roof}^* (in)$	normalized inflow rate across street roofs by downward flows
542	$Q_{roof}^* (out)$	normalized outflow rate across street roofs by upward outflows
543	S_c	pollutant release rate
544	S_α	turbulent Schmidt number
545	σ_w	fluctuation velocity on street roofs
546	τ_p, τ_p^*	age of air (s) and its normalized value
547	$\langle \tau_p^* \rangle$	normalized spatial mean age of air
548	U_m, I_m	velocity, turbulence intensity measured in upstream free flow
549	$U_0(z)$	velocity profiles used at CFD domain inlet for ventilation cases
550	U_H	reference velocity (2.66m/s) at $z=H$
551	\bar{u}_j, x_j	velocity and coordinate components
552	\bar{v}	velocity vector
553	Vol	control volume
554	x, y, z	stream-wise, span-wise, vertical directions

555

556 **References**

- 557 [1] Oke TR. Street design and urban canopy layer climate. *Energ Build* 1988; 11(1-3): 103-113.
- 558 [2] Bady M, Kato S, Huang H. Towards the application of indoor ventilation efficiency indices
- 559 to evaluate the air quality of urban areas. *Build Environ* 2008; 43(12): 1991-2004.

- 560 [3] Deng Q, He G, Lu C, Liu W. Urban ventilation - a new concept and lumped model. *Int J*
561 *Vent* 2012; 11: 131-140.
- 562 [4] Yang, XY, Li YG, Yang LN. Predicting and understanding temporal 3D exterior surface
563 temperature distribution in an ideal courtyard. *Build Environ* 2012; 57:38-48.
- 564 [5] Kato S, Murakami S, Takahashi T, Gyobu T. Chained analysis of wind tunnel test
565 and CFD on cross ventilation of large-scale market building. *J Wind Eng Ind Aerodyn* 1997; 67-
566 68: 573-587.
- 567 [6] da Graça GC, Martins NR, Horta CS. Thermal and airflow simulation of a naturally
568 ventilated shopping mall. *Energ Build* 2012; 50: 177-188.
- 569 [7] Kim T, Kim K, Kim BS. A wind tunnel experiment and CFD analysis on airflow
570 performance of enclosed-arcade markets in Korea. *Build Environ* 2010; 45: 1329-1338.
- 571 [8] Hang J, Li Y, Sandberg M, Buccolieri R, Di Sabatino S. The influence of building height
572 variability on pollutant dispersion and pedestrian ventilation in idealized high-rise urban areas.
573 *Build Environ* 2012; 56: 346-360.
- 574 [9] Hu T, Yoshie R. Indices to evaluate ventilation efficiency in newly-built urban area at
575 pedestrian level. *J Wind Eng Ind Aerodyn* 2013; 112: 39–51.
- 576 [10]Buccolieri R, Sandberg M, Di Sabatino S. City breathability and its link to pollutant
577 concentration distribution within urban-like geometries. *Atmos Environ* 2010; 44(15): 1894-
578 1903.
- 579 [11]Hang J, Li Y, Buccolieri R, Sandberg M, Di Sabatino S. On the contribution of mean flow
580 and turbulence to city breathability: the case of long streets with tall buildings. *Sci Total Environ*
581 2012; 416: 363-373.
- 582 [12]Britter RE, Hanna SR. Flow and dispersion in urban areas. *Annu Rev Fluid Mech* 2003;
583 35:469-496.
- 584 [13] Arnfield AJ. Two decades of urban climate research: a review of turbulence, exchanges of
585 energy and water, and the urban heat island. *Int J Climato* 2003; 23:1-26.
- 586 [14] Grimmond CSB, Blackett M, Best MJ, Barlow J, Baik JJ, Belcher SE et al. The
587 International Urban Energy Balance Models Comparison Project: First Results from Phase 1. *J*
588 *Appl Meteorol Clim* 2010; 49: 1268-1292.
- 589 [15] Li XX, Liu CH, Leung DY, Lam KM. Recent progress in CFD modelling of wind field
590 and pollutant transport in street canyons. *Atmos Environ* 2006; 40(29): 5640-5658.

- 591 [16] Meroney RN, Pavegeau M, Rafailidis S, Schatzmann M. Study of line source characteristics
592 for 2-D physical modelling of pollutant dispersion in street canyons. *J Wind Eng Ind Aerodyn*
593 1996; 62(1):37-56.
- 594 [17] Li XX, Liu CH, Leung DY. Numerical investigation of pollutant transport characteristics
595 inside deep urban street canyons. *Atmos Environ* 2009; 43(15): 2410-2418.
- 596 [18] Salim SM, Cheah SC, Chan A. Numerical simulation of dispersion in urban street canyons
597 with avenue-like tree plantings: Comparison between RANS and LES. *Build Environ* 2011;
598 46(9): 1735-1746.
- 599 [19] Cai XM. Effects of differential wall heating in street canyons on dispersion and ventilation
600 characteristics of a passive scalar. *Atmos Environ* 2012; 51: 268-277.
- 601 [20] Di Sabatino S, Buccolieri R, Pulvirenti B, Bitter R. Simulations of pollutant dispersion
602 within idealised urban-type geometries with CFD and integral models. *Atmos Environ* 2007;
603 41(37):8316-8329.
- 604 [21] Kanda M. Large-eddy simulations on the effects of surface geometry of building arrays on
605 turbulent organized structures. *Boundary-layer meteorol* 2006; 18(1): 151-168.
- 606 [22] Zaki SA, Hagishima A, Tanimoto J, Ikegaya N. Aerodynamic Parameters of Urban
607 Building Arrays with Random Geometries. *Boundary-Layer Meteorol* 2011; 138:99-120.
- 608 [23] Abd Razak A, Hagishima A, Ikegaya N, Tanimoto J. Analysis of airflow over building
609 arrays for assessment of urban wind environment. *Build Environ* 2013; 59:56-65.
- 610 [24] Yim SHL, Fung JCH, Lau AKH, Kot SC. Air ventilation impacts of the “wall effect”
611 resulting from the alignment of high-rise buildings. *Atmos Environ* 2009; 43(32): 4982-4994.
- 612 [25] Hagishima A, Tanimoto J, Nagayama K, Meno S. Aerodynamic parameters of regular
613 arrays of rectangular blocks with various geometries. *Boundary-Layer Meteorol* 2009;
614 132(2):315-337.
- 615 [26] Gu ZL, Zhang YW, Cheng Y, Lee SC. Effect of uneven building layout on air flow and
616 pollutant dispersion in non-uniform street canyons. *Build Environ* 2011; 46(12): 2657-2665.
- 617 [27] Chen Q. Ventilation performance prediction for buildings: a method overview and recent
618 applications. *Build Environ* 2009; 44:848-858.
- 619 [28] Luo ZW, Li YG. Passive urban ventilation by combined buoyancy-driven slope flow and
620 wall flow: Parametric CFD studies on idealized city models. *Atmos Environ* 2011; 45(32):5946-
621 5956.

- 622 [29] Yang LN, Li YG. Thermal conditions and ventilation in an ideal city model of Hong Kong.
623 *Energ Buildings* 2011; 43(5): 1139-1148.
- 624 [30] Hang J, Li YG. Wind conditions in idealized building clusters--macroscopic simulations by a
625 porous turbulence model. *Boundary-Layer Meteorol* 2010; 136(1): 129-159.
- 626 [31] Liu CH, Cheng WC, Leung TCY, Leung DYC. On the mechanism of air pollutant re-
627 entrainment in two-dimensional idealized street canyons. *Atmos Environ* 2011; 45(27) : 4763-
628 4769.
- 629 [32] Hang J, Sandberg M, Li YG. Age of air and air exchange efficiency in idealized city models.
630 *Build Environ* 2009; 44(8):1714-1723.
- 631 [33] Santiago JL, Dejoan A, Martilli A, Martin F, Pinelli A. Comparison between Large-Eddy
632 Simulation and Reynolds-Averaged Navier–Stokes computations for the MUST field
633 experiment. Part I: study of the flow for an incident wind directed perpendicularly to the front
634 array of containers. *Boundary-Layer Meteorol* 135; 2010:109-132.
- 635 [34] Salim SM, Buccolieri R, Chan A, Di Sabatino S. Numerical simulation of atmospheric
636 pollutant dispersion in an urban street canyon: Comparison between RANS and LES. *J Wind
637 Eng Ind Aerodyn* 2011; 99(2-3): 103-113.
- 638 [35] Yoshie R, Mochida A, Tominaga Y, Kataoka H, Harimoto K, Nozu T, Shirasawa T.
639 Cooperative project for CFD prediction of pedestrian wind environment in the Architectural
640 Institute of Japan. *J Wind Eng Ind Aerodyn* 2007; 95:1551-1578.
- 641 [36] Mochida A, Lun IYF. Prediction of wind environment and thermal comfort at pedestrian
642 level in urban area. *J Wind Eng Ind Aerodyn* 2008; 96(10-11): 1498-1527.
- 643 [37] Hang J, Sandberg M, Li Y. Effect of urban morphology on wind condition in idealized city
644 models. *Atmos Environ* 2009; 43(4): 869-878.
- 645 [38] FLUENT V6.3. User's Manual.2006. <http://www.fluent.com>.
- 646 [39] Snyder WH. Similarity criteria for the application of fluid models to the study of air
647 pollution meteorology. *Boundary-Layer Meteorol* 1972; 3:113-134.
- 648 [40] Tominaga Y, Mochida A, Yoshie R, Kataoka H, Nozu T, Yoshikawa M, Shirasawa T. AIJ
649 guidelines for practical applications of CFD to pedestrian wind environment around buildings. *J
650 Wind Eng Ind Aerodyn* 2008; 96(10-11):1749-1761.

651 [41] Lien FS, Yee E. Numerical modelling of the turbulent flow developing within and over a 3-
652 D building array, part I: A high-resolution Reynolds-averaged Navier-Stokes approach.
653 *Boundary-layer Meteorol* 2004; 112(3): 427-466.

654 [42] Irwin JS. A theoretical variation of the wind profile power-law exponent as a function of
655 surface roughness and stability. *Atmos Environ* 1979; 13(1):191-194.

656 [43]WMO Guide to Meteorological Instruments and Methods of Observation WMO-No. 8, page
657 I.5-12

658 [44]Etheridge D, Sandberg M. *Building Ventilation: Theory and Measurement*. John Wiley &
659 Sons, Chichester. 1996, p.573-633.

660 [45] Tominaga Y, Stathopoulos T. Turbulent Schmidt numbers for CFD analysis with various
661 types of flow field. *Atmos Environ* 2007; 41(37):8091-8099.

662

663 **Figure list**

664 Fig. 1. Two urban configurations of semi-open street roof design: (a) Walls being hung above
665 street roofs of food court, (b) Walls being partly covered by street roof height ($z=H$) of retail
666 center.

667

668 Fig. 2. Model descriptions of experimental model: (a) The idealized urban model with 4
669 buildings and open street roof, (b) Vertical profiles of velocity and turbulence intensity in the
670 upstream free flow of wind tunnel experiment.

671

672 Fig. 3. (a) Computational domain for cases with a parallel approaching wind (0°) and half domain
673 size, (b) Grid arrangements in x - y plane in the validation case.

674

675 Fig. 4. (a) Computational domain with oblique wind direction and full domain size. Model
676 descriptions of urban models with (b) 4 (2×2) buildings and (c) 16 (4×4) buildings.

677

678 Fig. 5. (a) 'Fully-covered' roof type: walls fully cover street roofs at $z=H$ (b) 'Partly-covered' roof
679 type: walls partly cover street roofs at $z=H$, (c) Types of 'Hung1.5H', 'Hung1.2H', 'Hung1.1H':
680 walls are hung above street roofs at $z=1.1H$, $1.2H$, $1.5H$.

681

682 Fig. 6. Two examples of grid arrangements for urban geometries with 4 buildings: (a) in x - y
 683 plane, (b) in x - z plane. (c) Definition of uniform pollutant source in UCL volume.

684

685 Fig. 7. Validation profiles of (a) velocity and (b) turbulence intensity along the street centerline
 686 at $z=0.11H$ by using different turbulence models. (c) Horizontal profiles of velocity for a grid
 687 independence study.

688

689 Fig. 8. (a) 3D streamline, (b) τ_p^* in $z=0.22H$ and Q^* in Case [2-2, 0, Open], Case [2-2, 0,
 690 Hung1.2H], Case [2-2, 0, Partly-covered], Case [2-2, 0, Fully-covered].

691

692 Fig. 9. (a) 3D streamline, (b) τ_p^* and Q^* in Case [2-2, 0, Hung1.5H], Case [2-2, 15, Hung1.5H],
 693 Case [2-2, 30, Hung1.5H], Case [2-2, 45, Hung1.5H]. Note that in Fig. 9b, negative values of Q^*
 694 by mean flows denote air leaving UCL and positive ones represent air entering UCL.

695

696 Fig. 10. Q^* in urban models with 4 buildings and wind directions of (a) 0° , (b) 15° , (c) 30° ,
 697 (d) 45° .

698

699 Fig. 11. Ventilation indices and their NVR for test cases with 4 buildings: (a) Q_{roof}^* (in) and
 700 Q_{roof}^* (out), (b) Q_{roof}^* (turb), (c) Q_T^* , (d) PFR^* , (e) $\langle \tau_p^* \rangle$.

701

702 Fig. 12. τ_p^* in $z=0.22H$ in (a) Case [4-4, 0, Hung1.2H], (b) Case [4-4, 15, Hung1.2H], (c) Case
 703 [4-4, 30, Hung1.2H], (d) Case [4-4, 45, Hung1.2H].

704

705 Fig. 13. Ventilation indices and their NVR : (a) Q_{roof}^* (in) and Q_{roof}^* (out) in 24 test cases with
 706 16 buildings, In all 48 test cases: (b) Q_{roof}^* (turb), (c) Q_T^* , (d) PFR^* , (e) $\langle \tau_p^* \rangle$.

Table 1 Model descriptions of 48 test cases.

2 rows, 2 columns (2×2)		4 rows, 4 columns (4×4)	
Case name*	Ambient wind direction θ°	Case name	Ambient wind direction θ°
[2-2, 0, Open]	0°	[4-4, 0, Open]	0°
[2-2, 0, Hung1.5H]		[4-4, 0, Hung1.5H]	
[2-2, 0, Hung1.2H]		[4-4, 0, Hung1.2H]	
[2-2, 0, Hung1.1H]		[4-4, 0, Hung1.1H]	
[2-2, 0,Partly-covered]		[4-4, 0,Partly-covered]	
[2-2, 0, Fully-covered]		[4-4, 0, Fully-covered]	
[2-2, 15, Open]	15°	[4-4, 15, Open]	15°
[2-2, 15, Hung1.5H]		[4-4, 15, Hung1.5H]	
[2-2, 15, Hung1.2H]		[4-4, 15, Hung1.2H]	
[2-2, 15, Hung1.1H]		[4-4, 15, Hung1.1H]	
[2-2, 15,Partly-covered]		[4-4, 15,Partly-covered]	
[2-2, 15, Fully-covered]		[4-4, 15, Fully-covered]	
[2-2, 30, Open]	30°	[4-4, 30, Open]	30°
[2-2, 30, Hung1.5H]		[4-4, 30, Hung1.5H]	
[2-2, 30, Hung1.2H]		[4-4, 30, Hung1.2H]	
[2-2, 30, Hung1.1H]		[4-4, 30, Hung1.1H]	
[2-2, 30,Partly-covered]		[4-4, 30,Partly-covered]	
[2-2, 30, Fully-covered]		[4-4, 30, Fully-covered]	
[2-2, 45, Open]	45°	[4-4, 45, Open]	45°
[2-2, 45, Hung1.5H]		[4-4, 45, Hung1.5H]	
[2-2, 45, Hung1.2H]		[4-4, 45, Hung1.2H]	
[2-2, 45, Hung1.1H]		[4-4, 45, Hung1.1H]	
[2-2, 45,Partly-covered]		[4-4, 45,Partly-covered]	
[2-2, 45, Fully-covered]		[4-4, 45, Fully-covered]	

*Case name is defined as [row number-column number, wind direction (θ°), roof type]. 'Open' denotes open street roofs; 'Fully-covered' and 'Partly-covered' means solid walls 'fully or 'partly cover' street roofs at $z=H$. 'Hung1.5H, Hung1.2H and Hung1.1H' represent solid walls are 'Hung' above street roofs at $z=1.5H, 1.2H$ and $1.1H$.

Table 2 Effect of turbulence models and turbulent Schmidt number (Sc_t) on $\langle \tau_p^* \rangle$, PFR^* and Q_T^* in the entire UCL, $Q_{roof}^*(turb)^*$ and Q^* across O3 in Case [2-2, 0, Open].

Turbulence models	Sc_t	$\langle \tau_p^* \rangle$	PFR^*	Q_T^*	$Q_{roof}^*(out)$	$Q_{roof}^*(in)$	$Q_{roof}^*(turb)$	$Q^*(O3)$
Standard $k-\varepsilon$	0.4	21.2	1.847	1.376	-0.825	0.148	1.211	-0.551
	0.7	24.3	1.609					
	1.0	26.4	1.482					
Realizable $k-\varepsilon$	0.7	27.2	1.439	1.401	-0.844	0.145	1.066	-0.536
RNG $k-\varepsilon$	0.7	28.8	1.358	1.378	-1.127	0.181	0.919	-0.274

*Negative values denote air leaving UCL and positive ones represent air entering it.



(a)



(b)

Fig. 1. Hang et al.

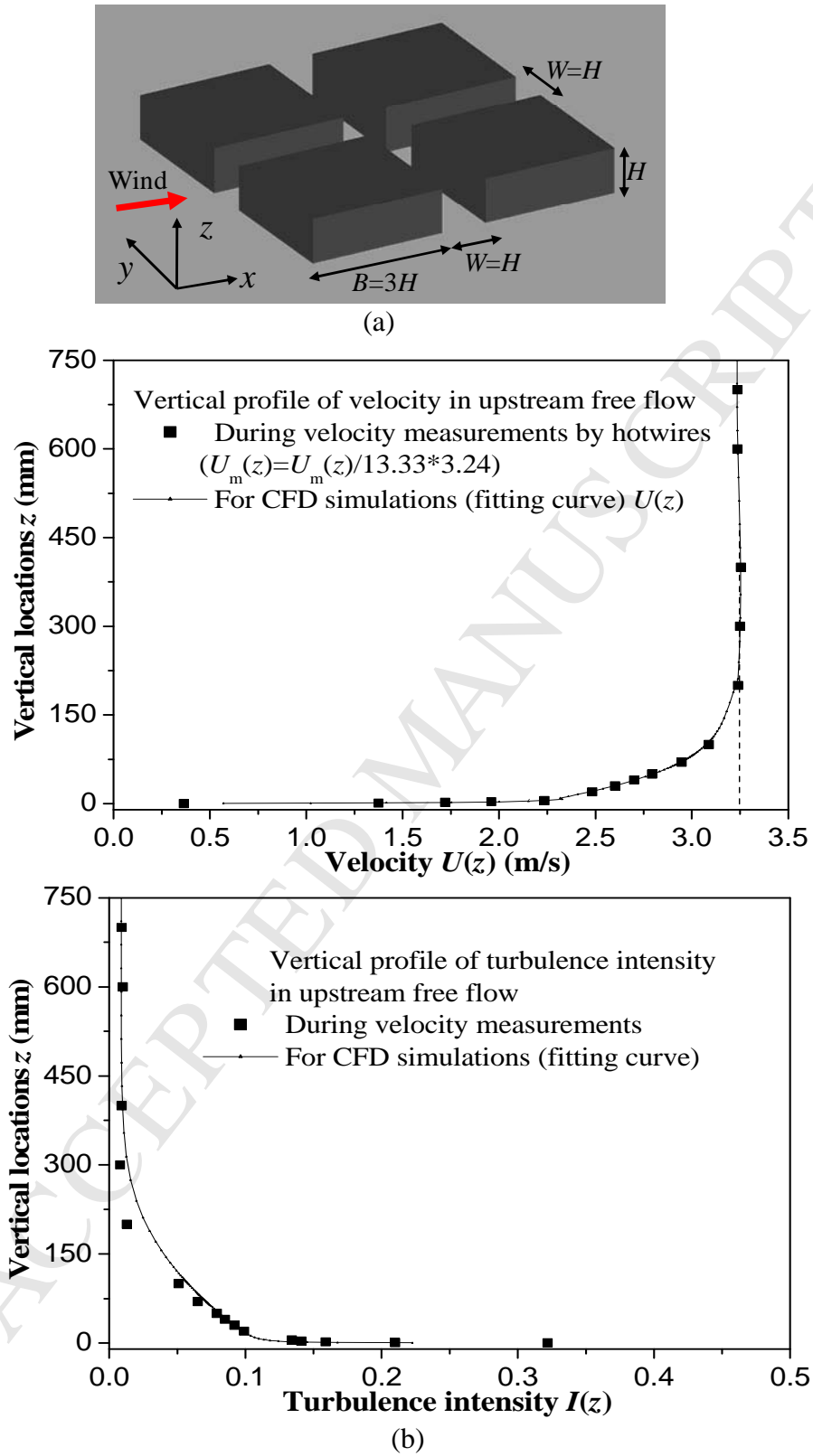


Fig. 2. Hang et al.

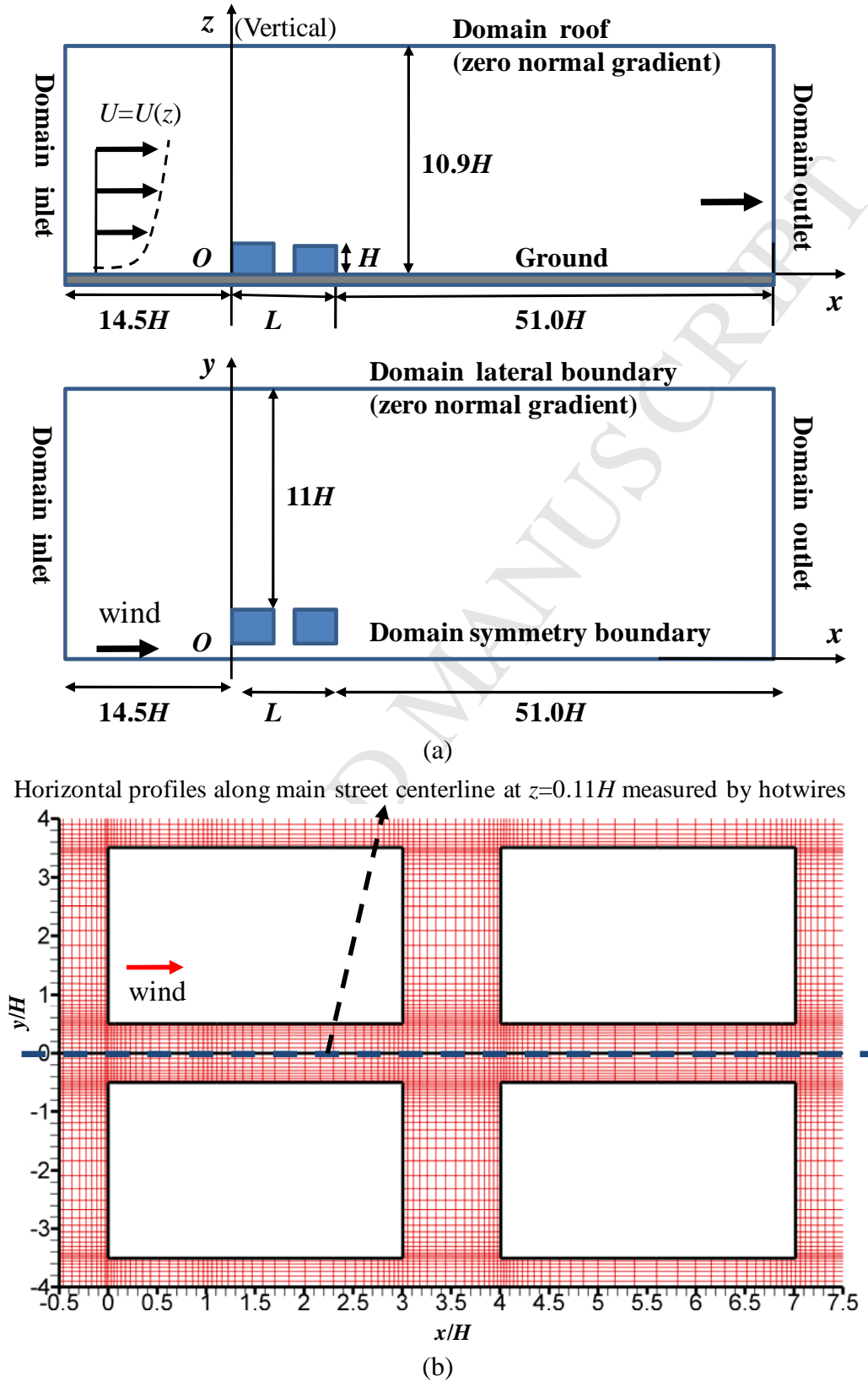
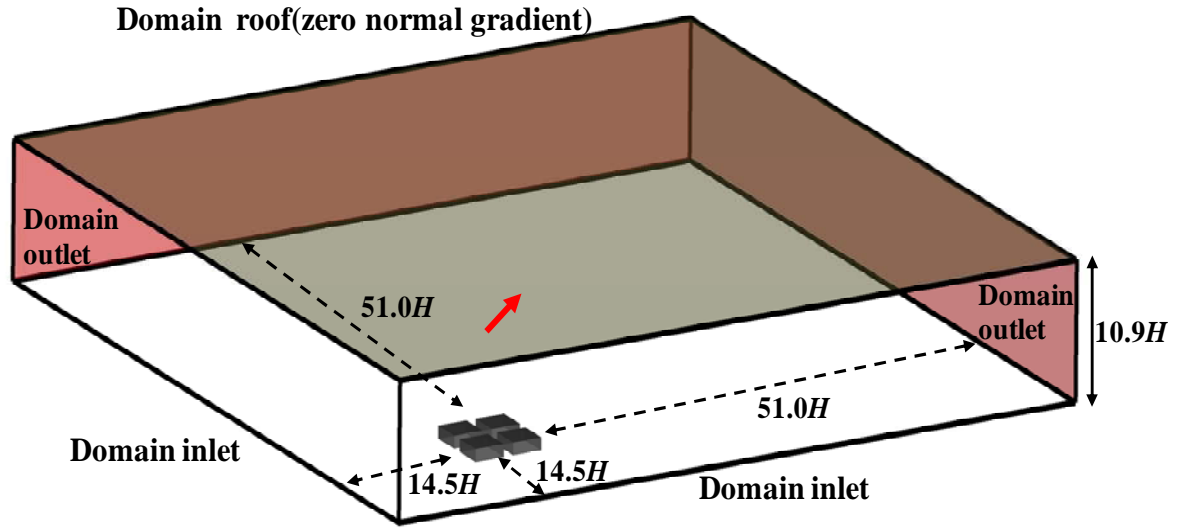
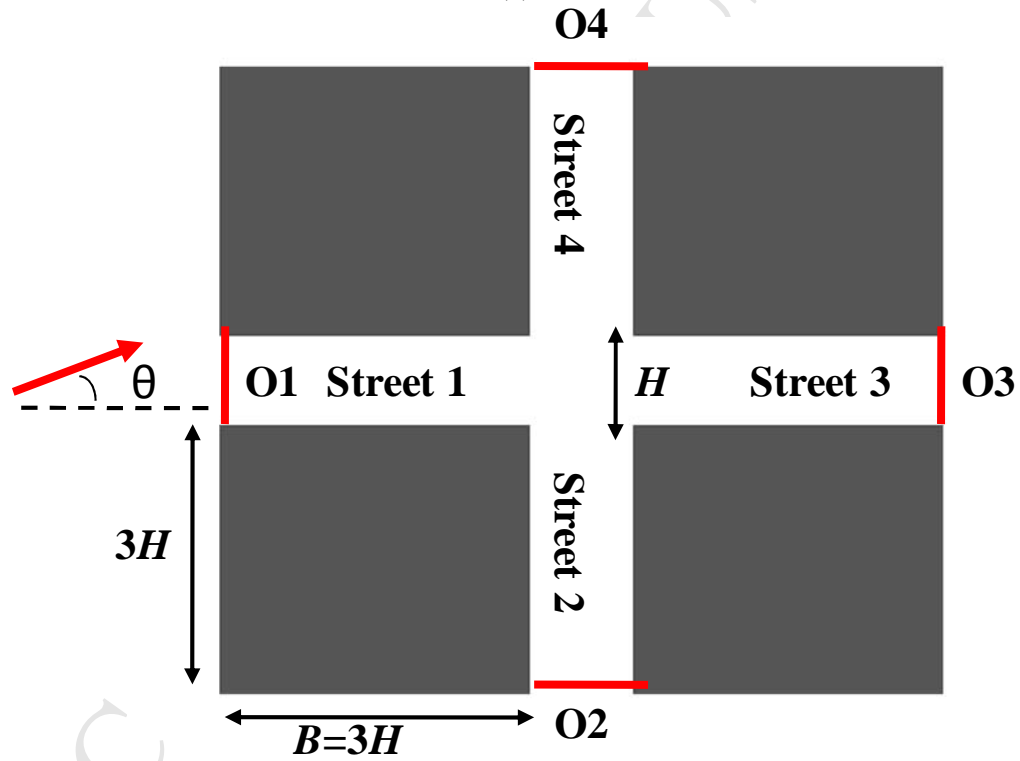


Fig. 3 Hang et al.



(a)



(b)

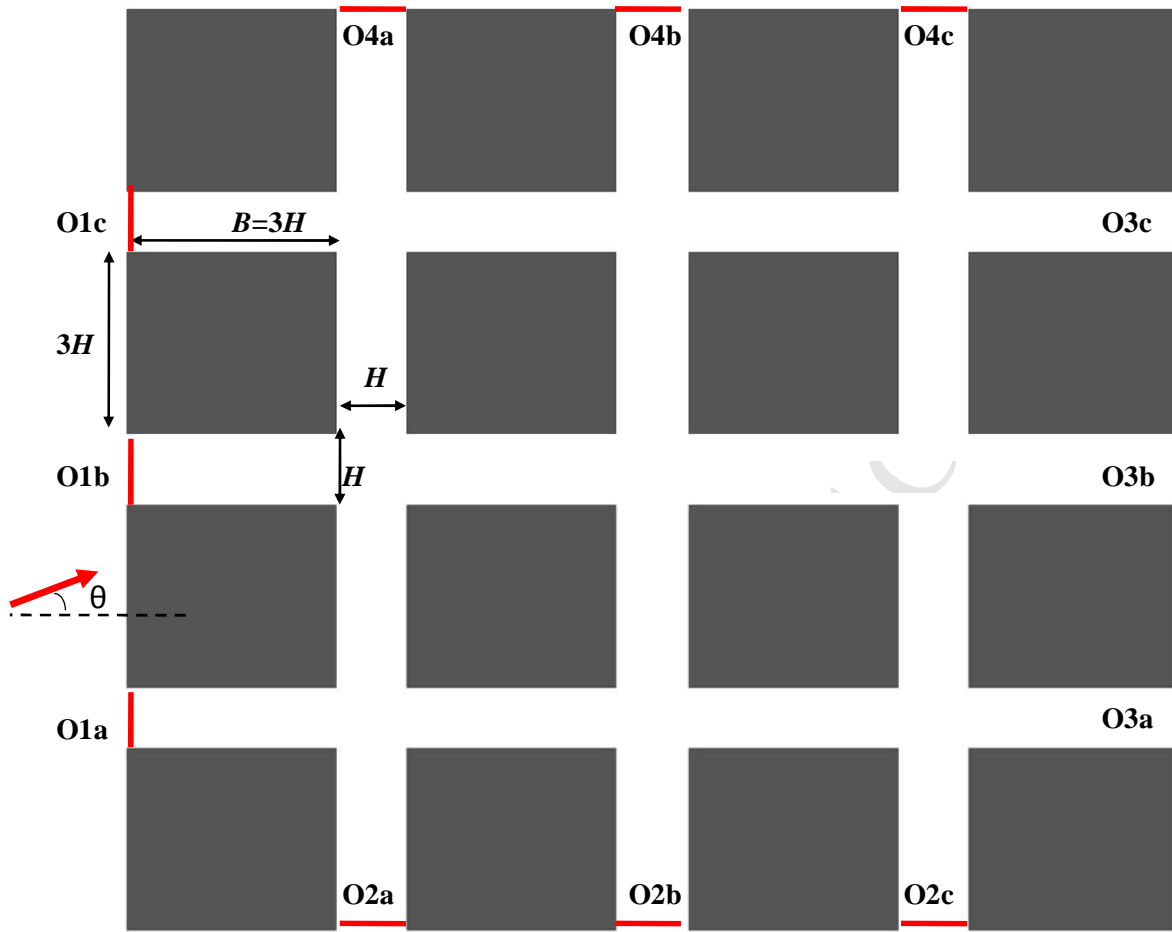
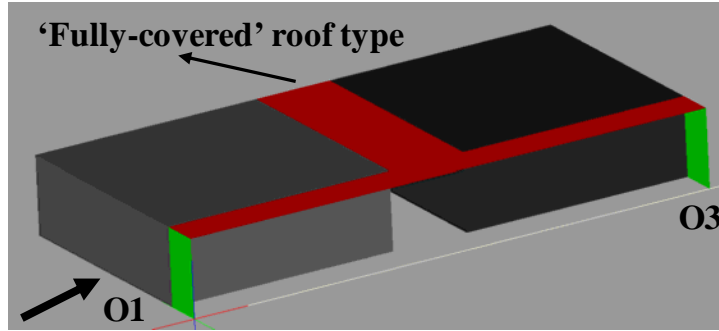
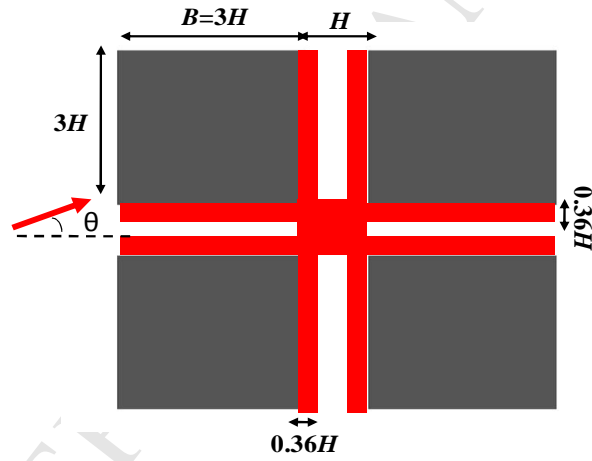
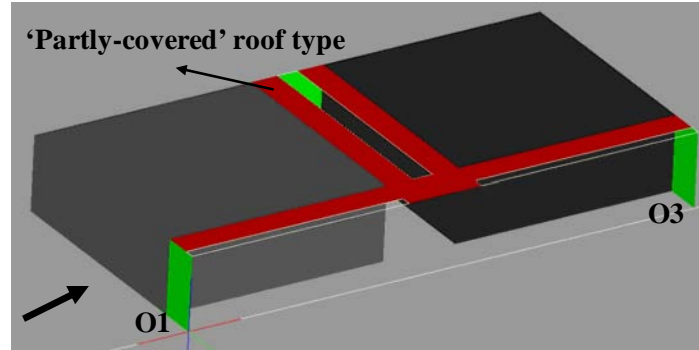


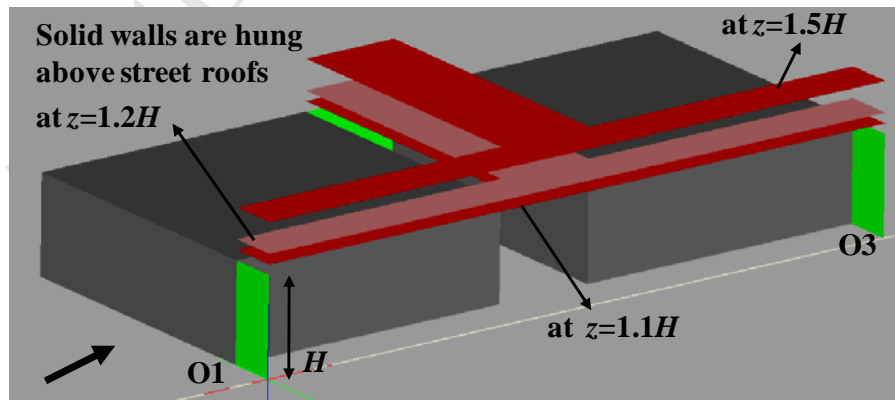
Fig. 4. Hang et al. (c)



(a) Enclosed street roof



(b)



(c)

Fig. 5. Hang et al.

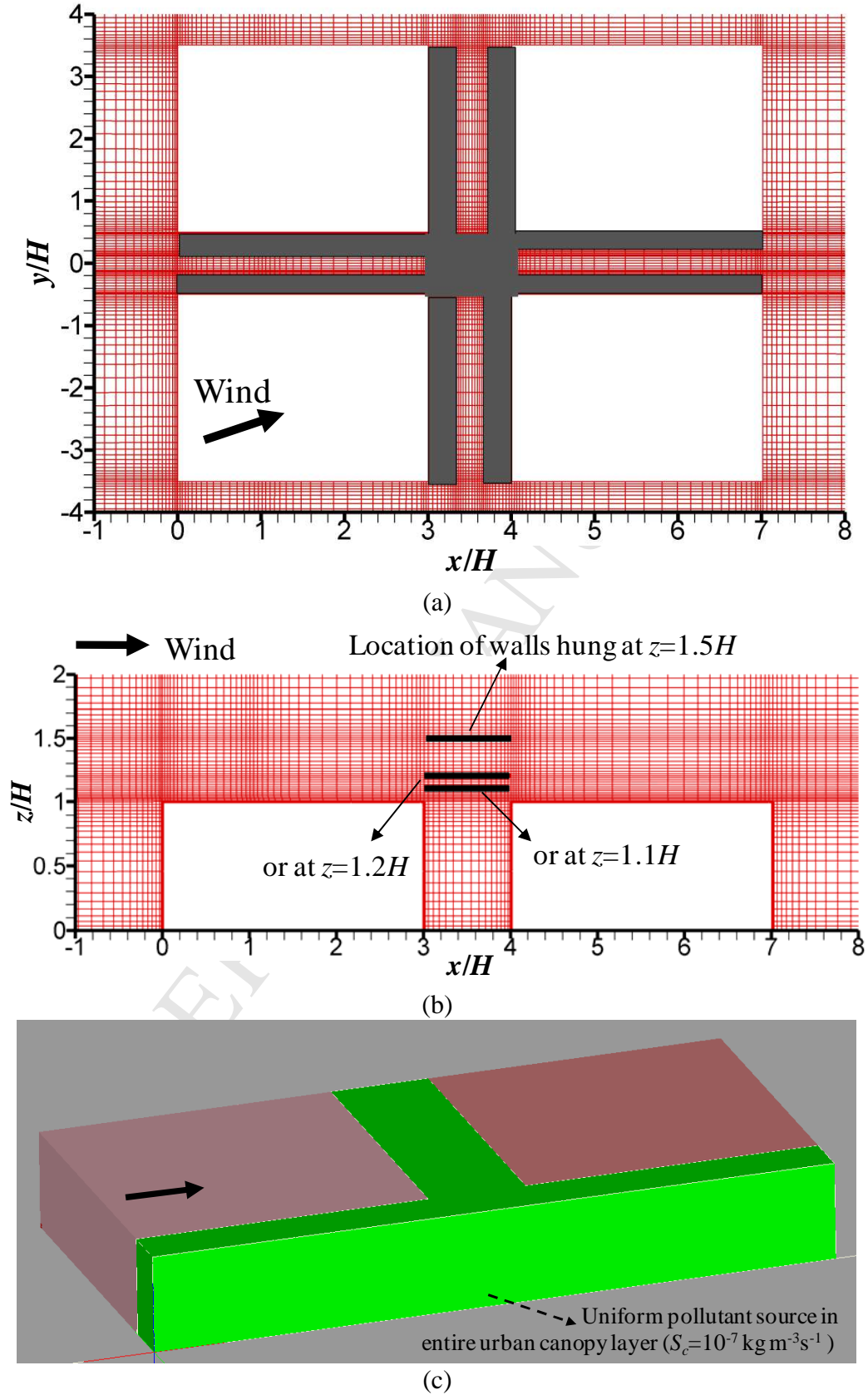


Fig.6. Hang et al.

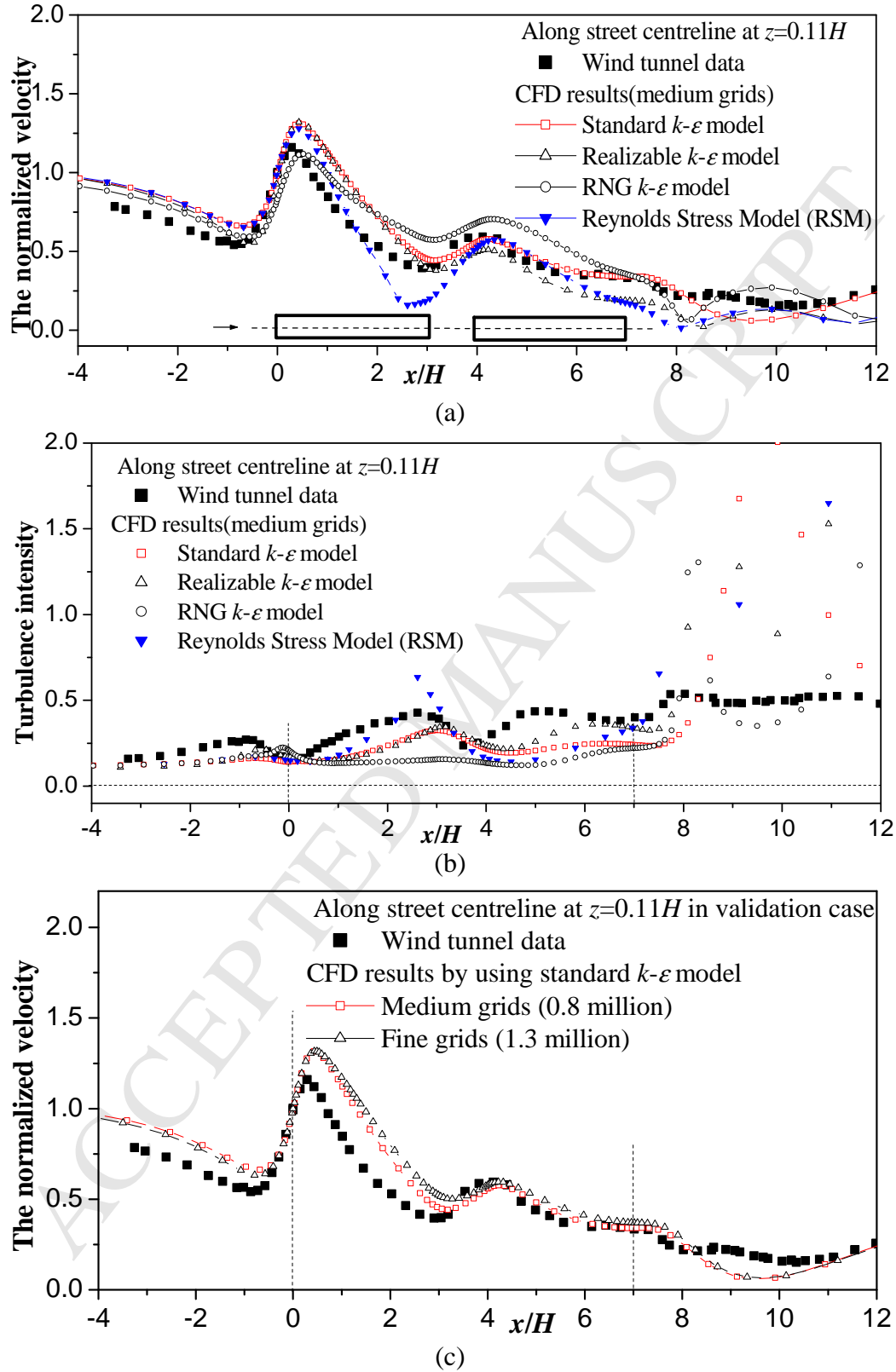
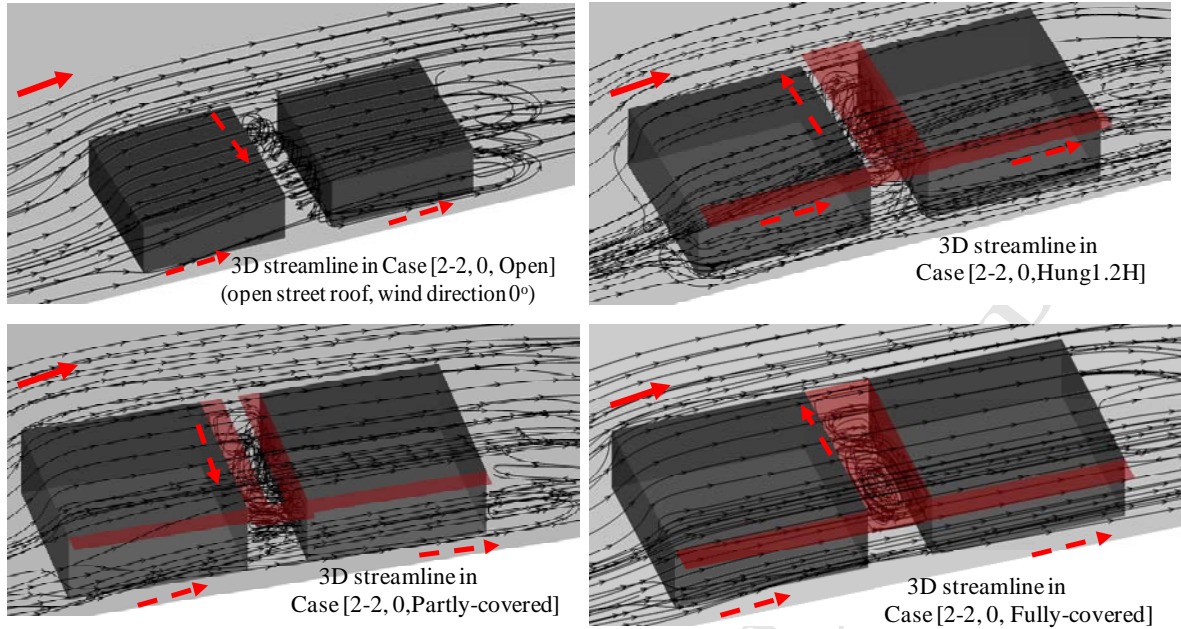
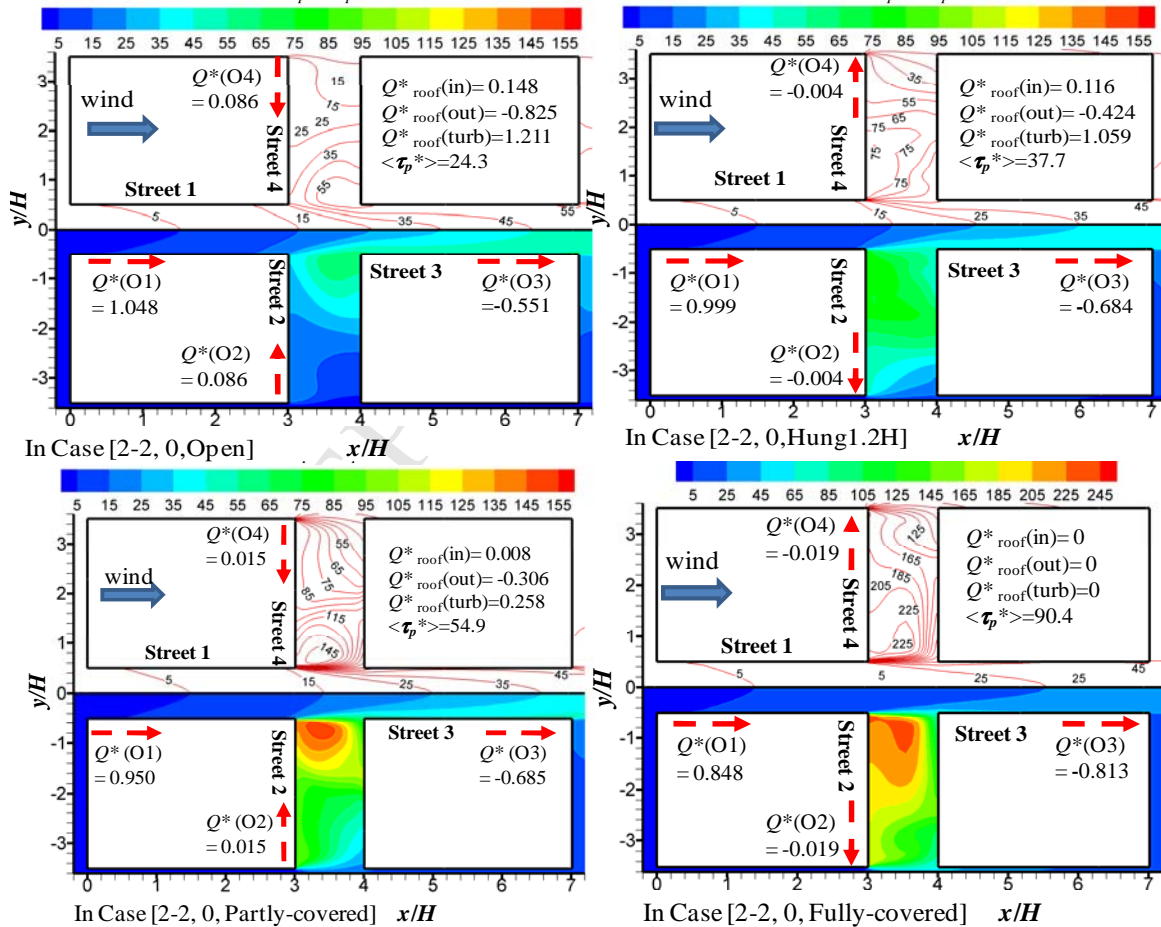


Fig. 7. Hang et al.

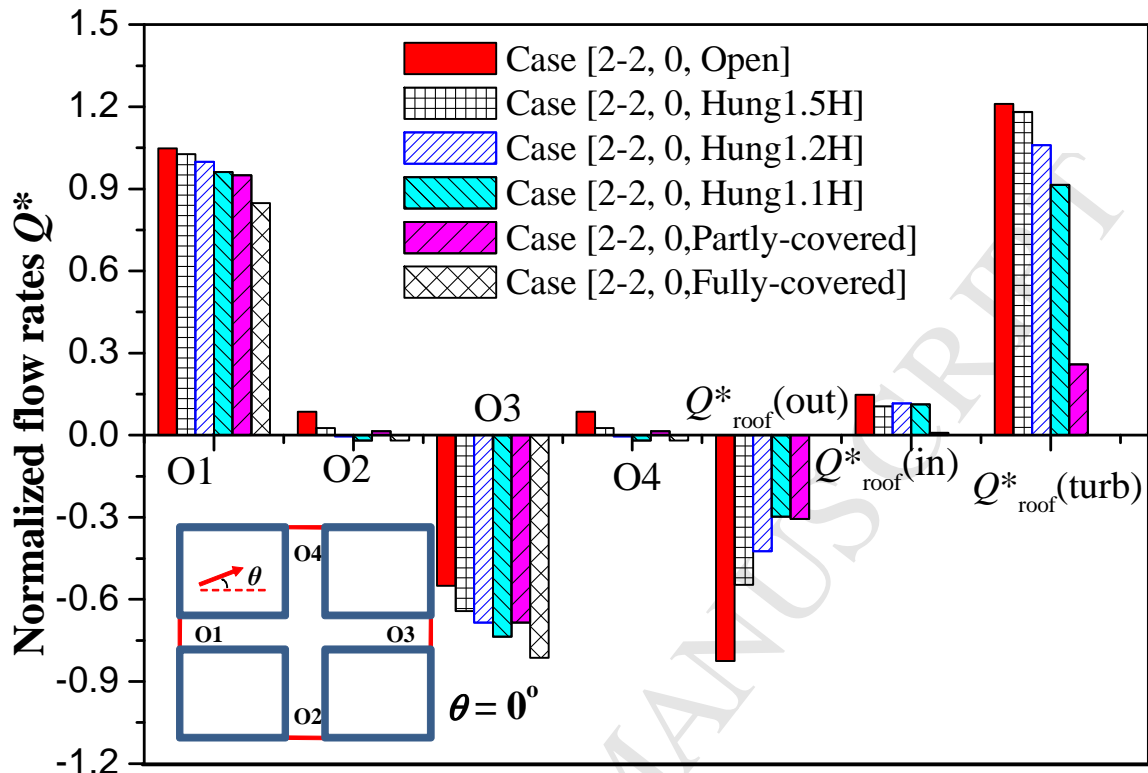


(a)

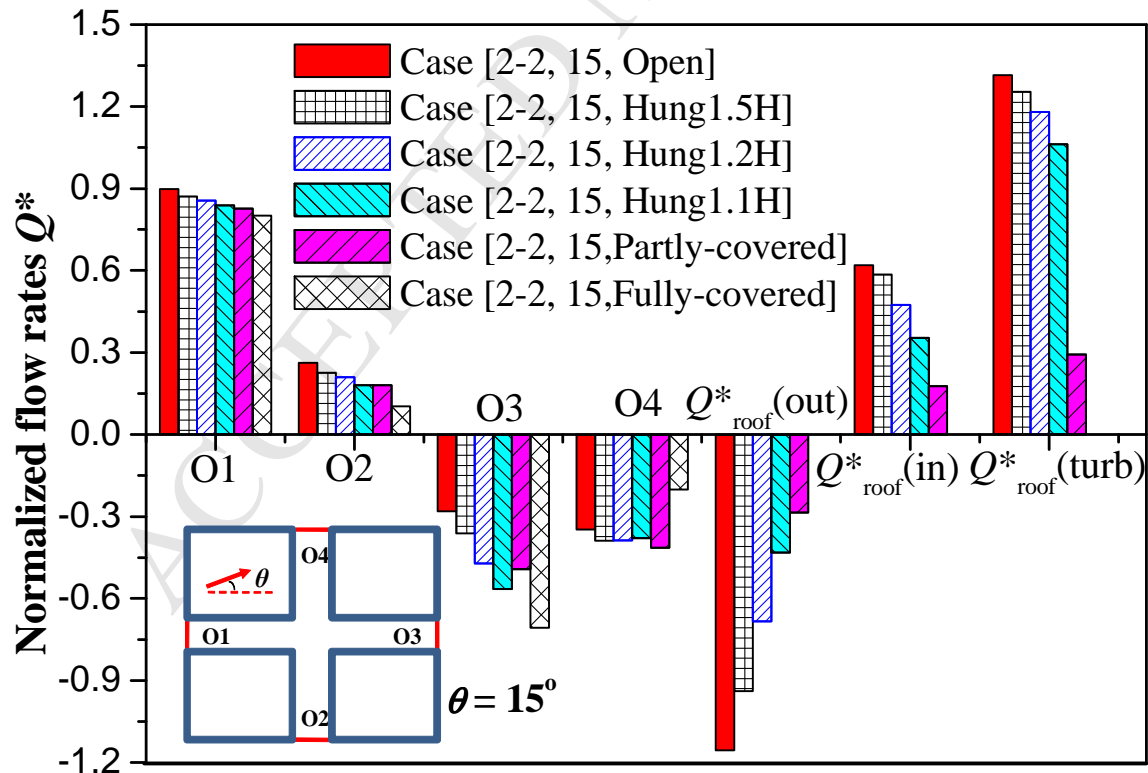
Normalized age of air ($\tau_p^* = \tau_p \times 100$ s) in $z=0.22H$ 

(b)

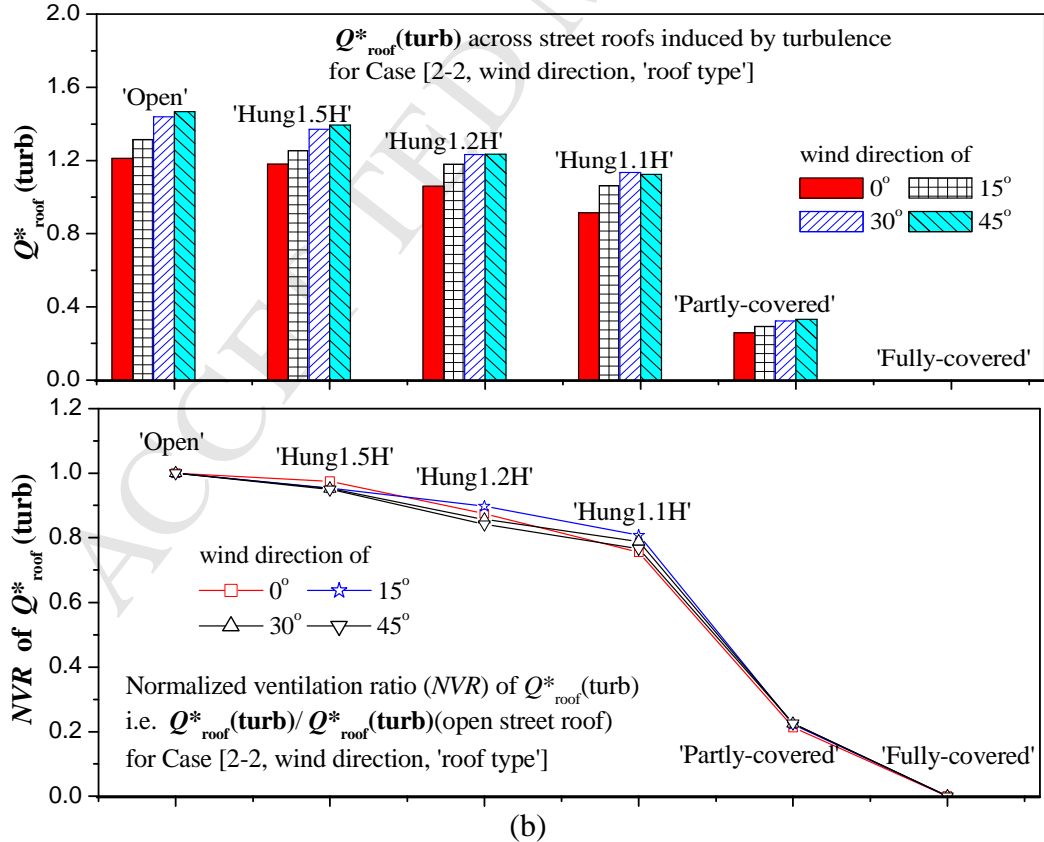
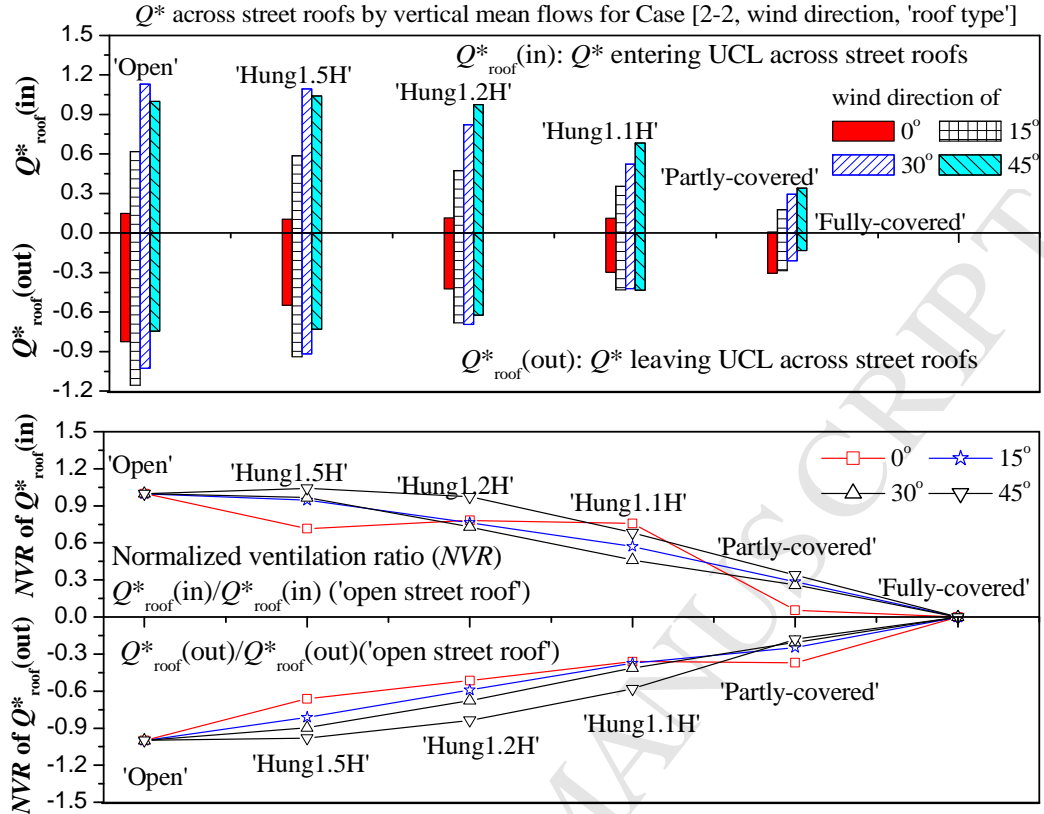
Fig. 8 Hang et al.

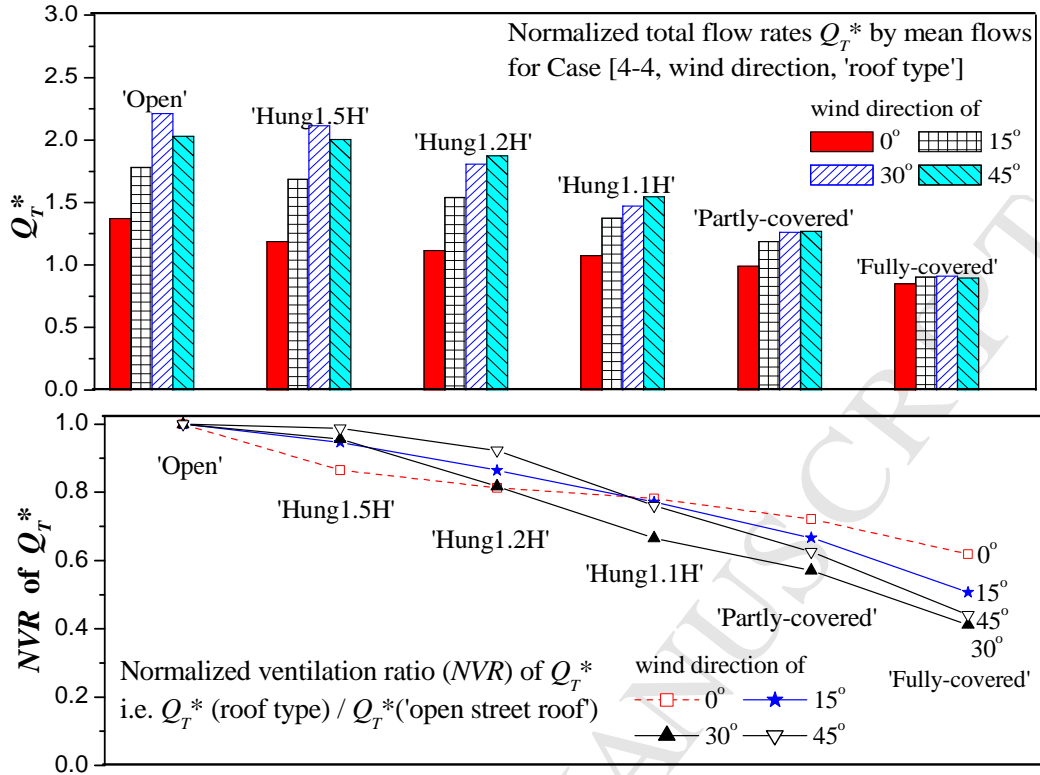


(a)

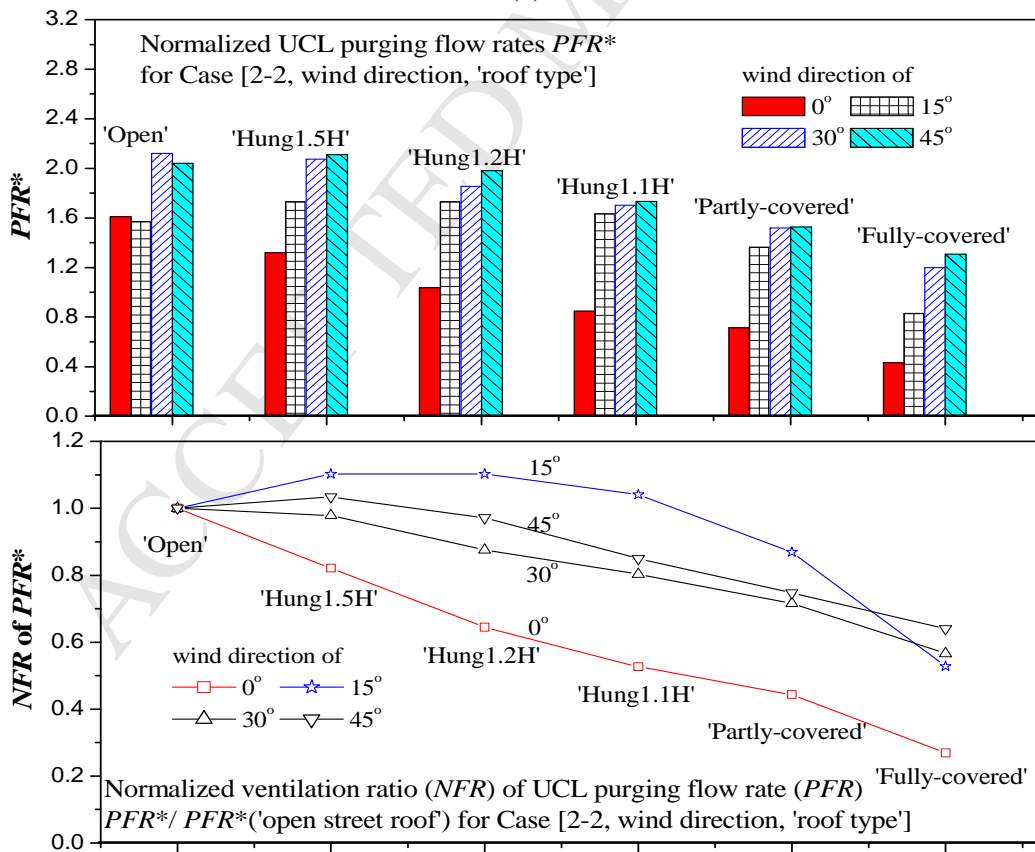


(b)





(c)



(d)

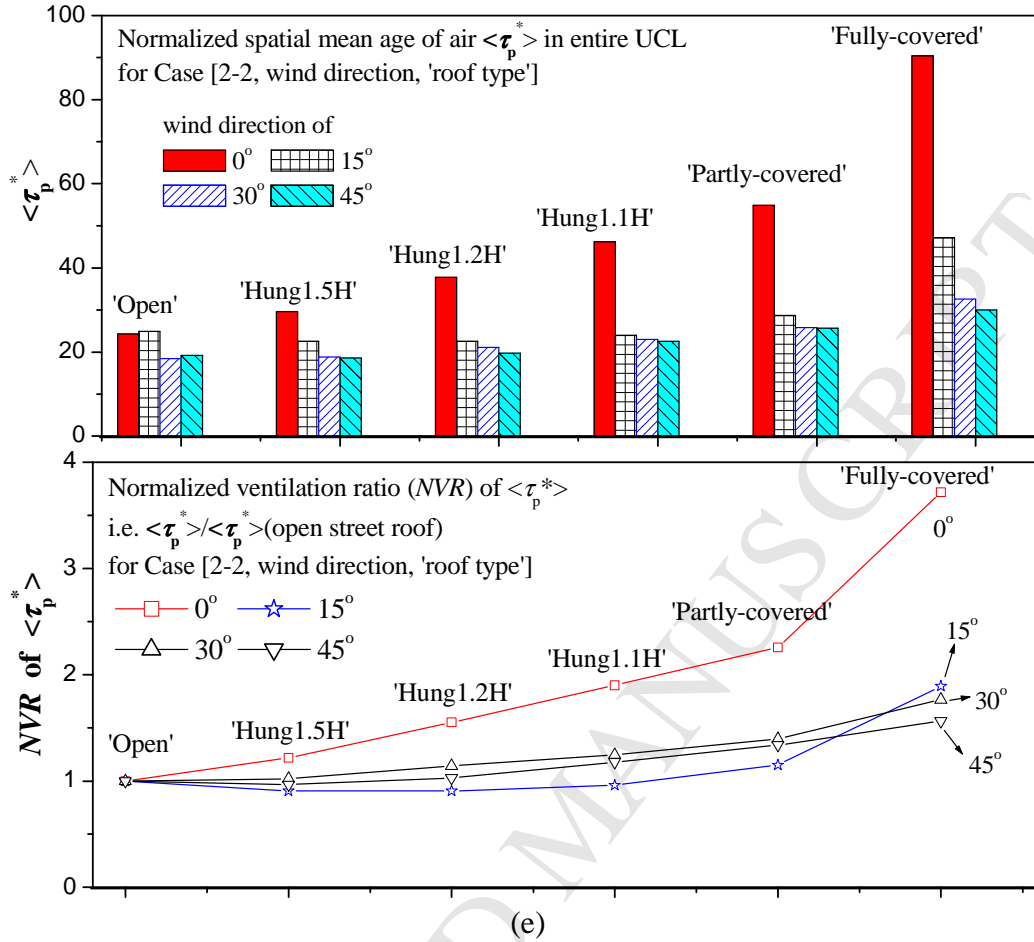
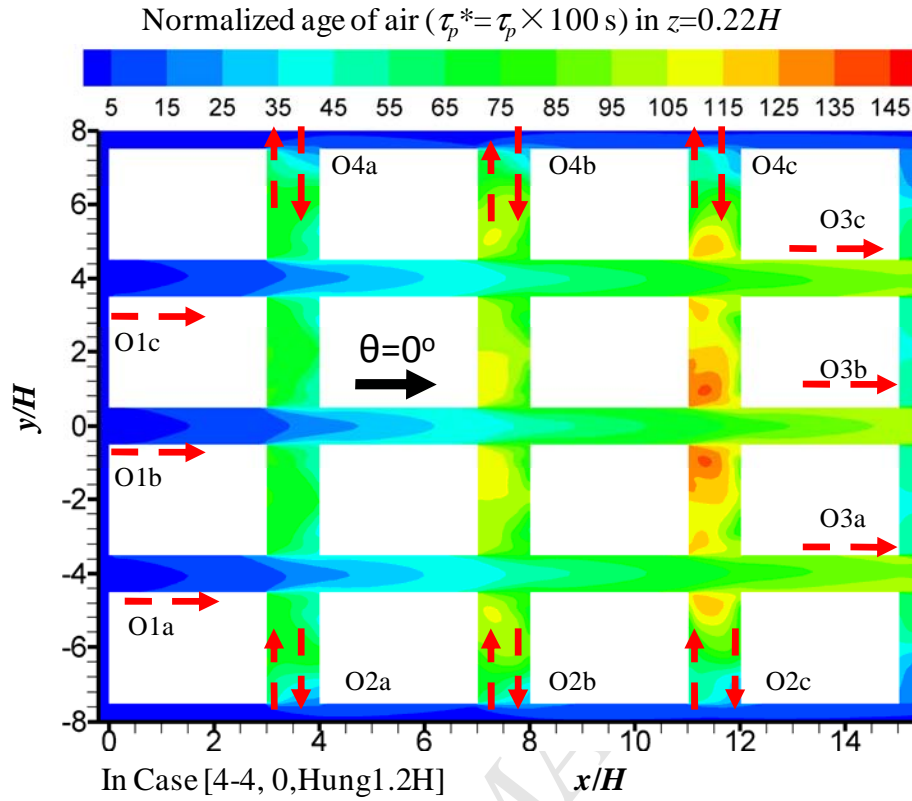
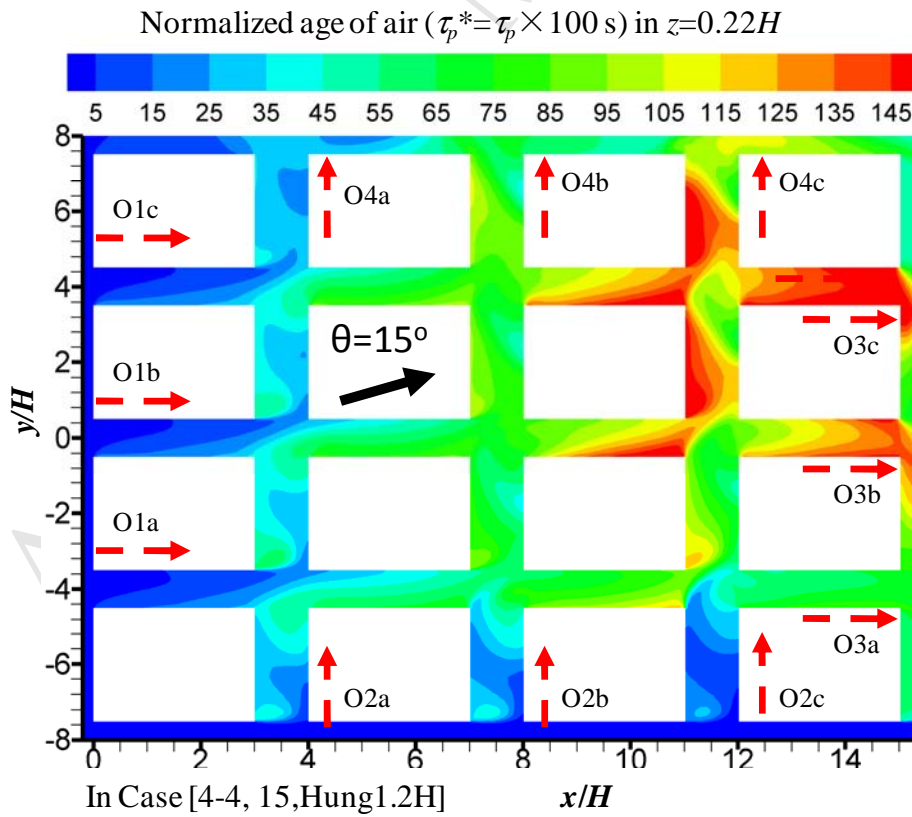


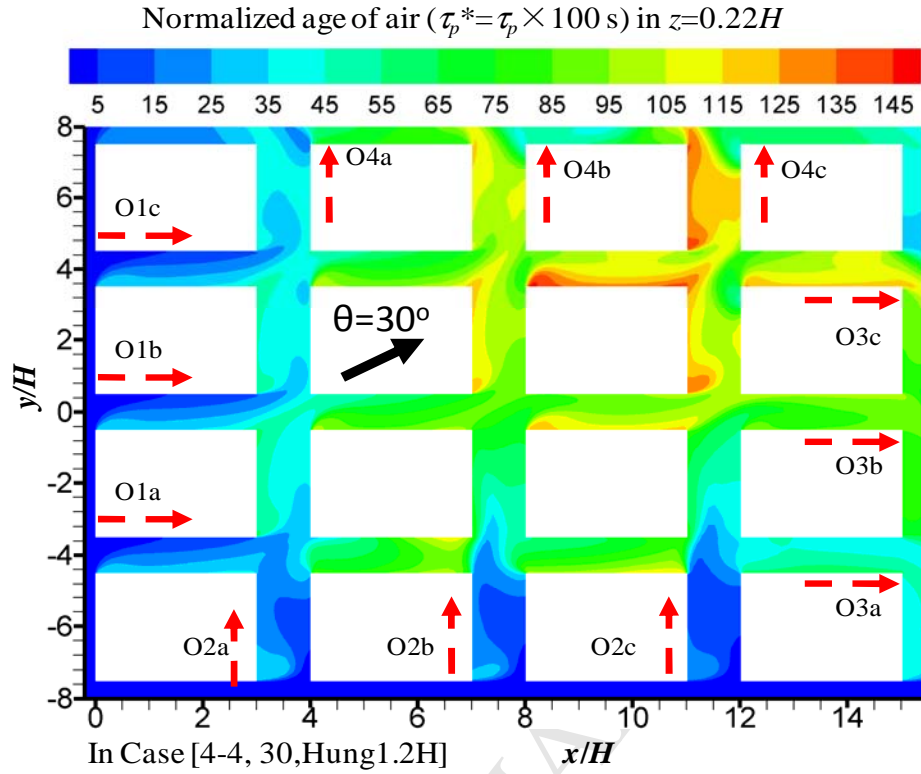
Fig. 11. Hang et al.



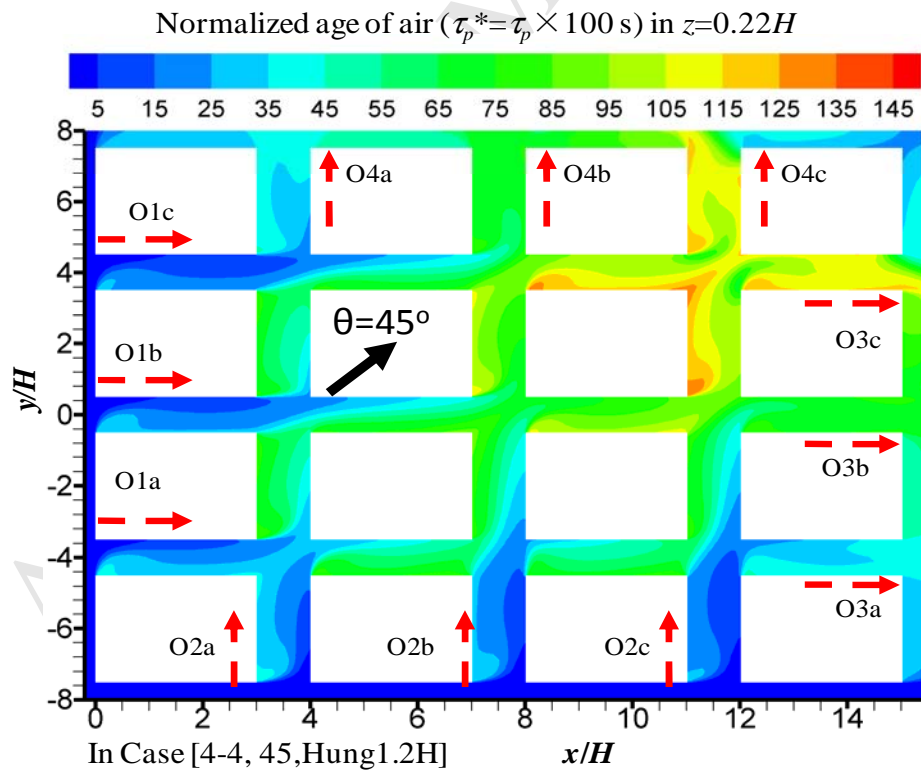
(a)



(b)

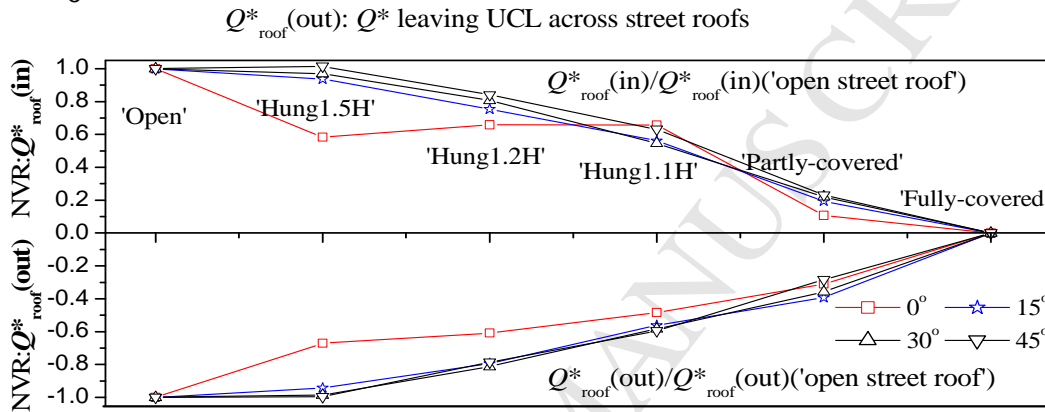
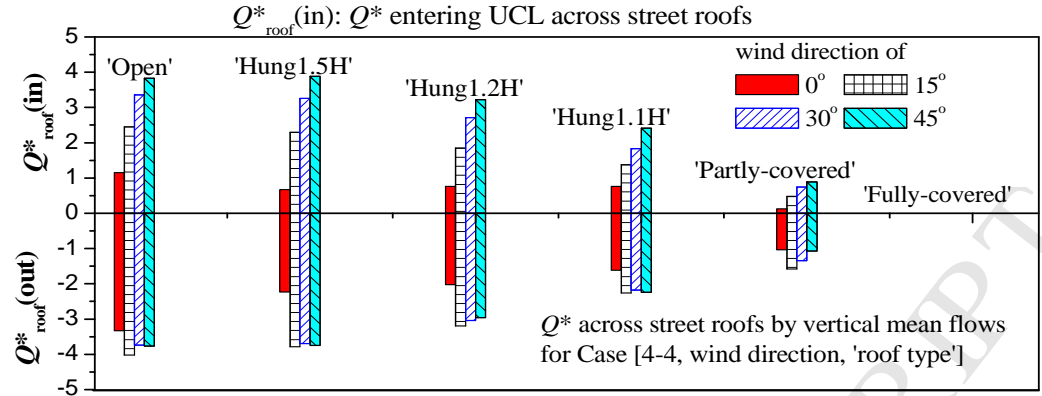


(c)

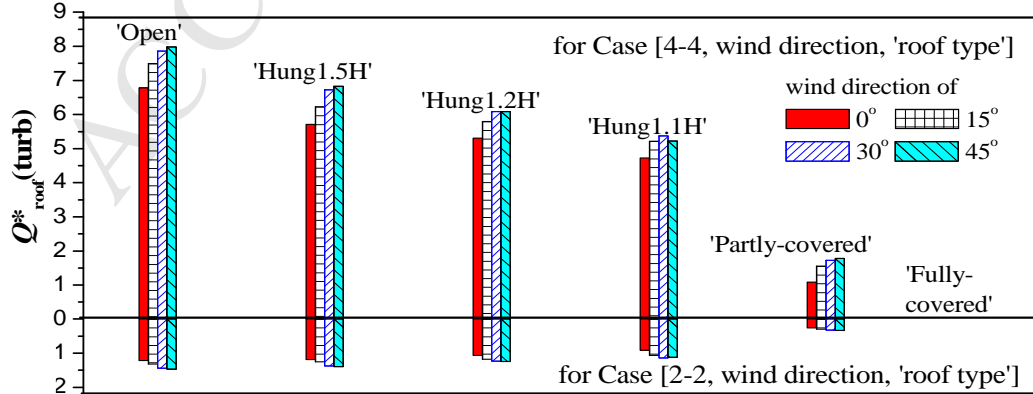
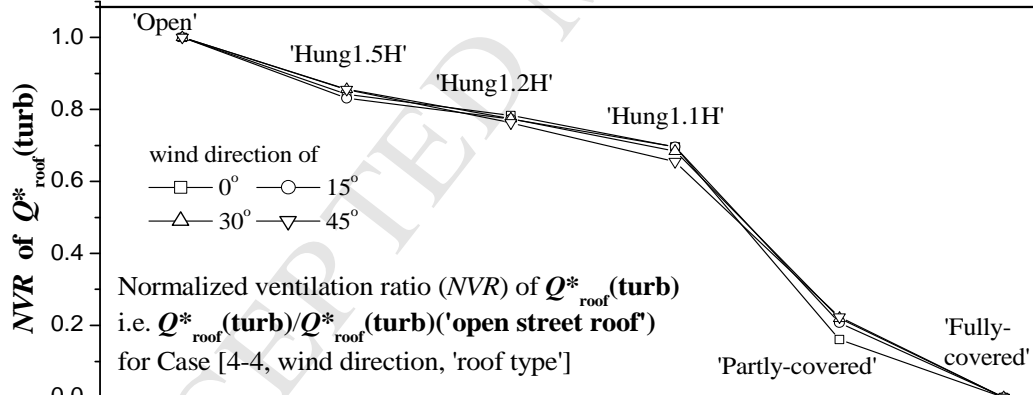


(d)

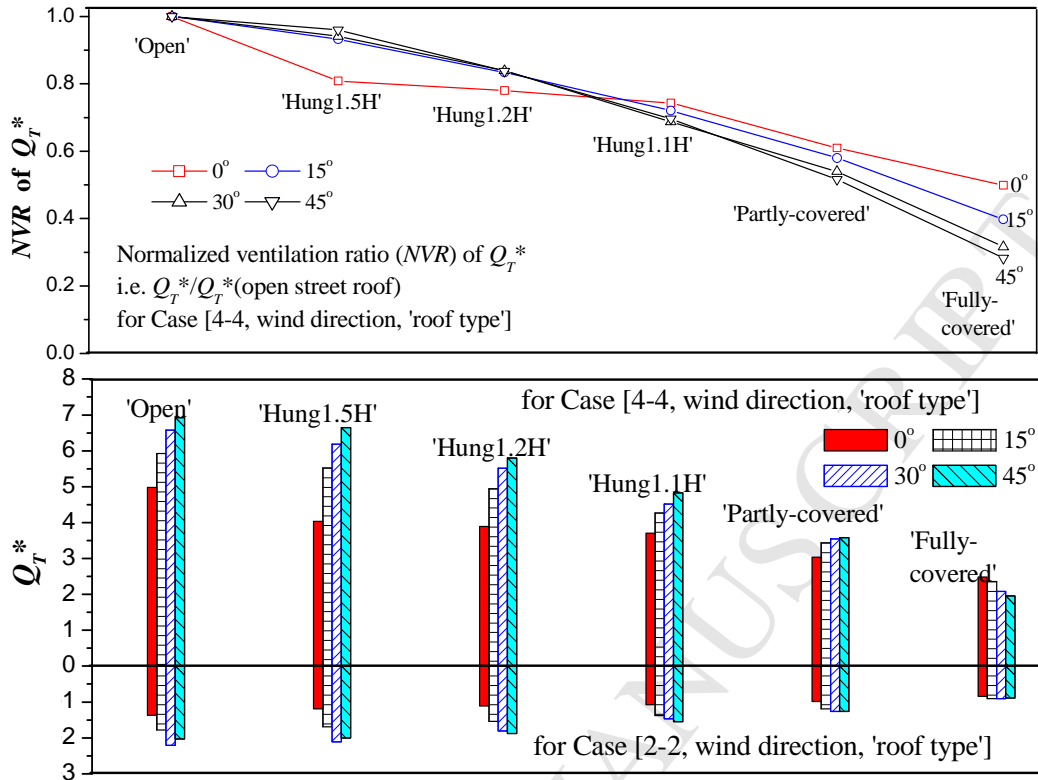
Fig. 12. Hang et al.



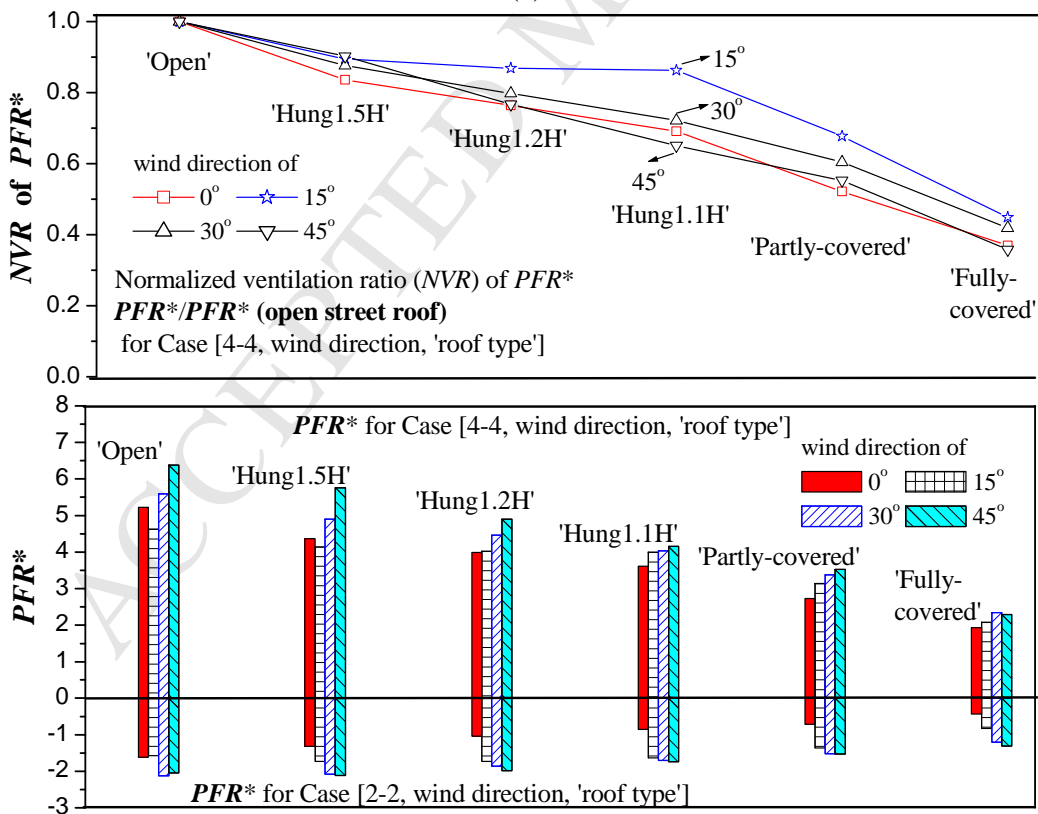
(a)



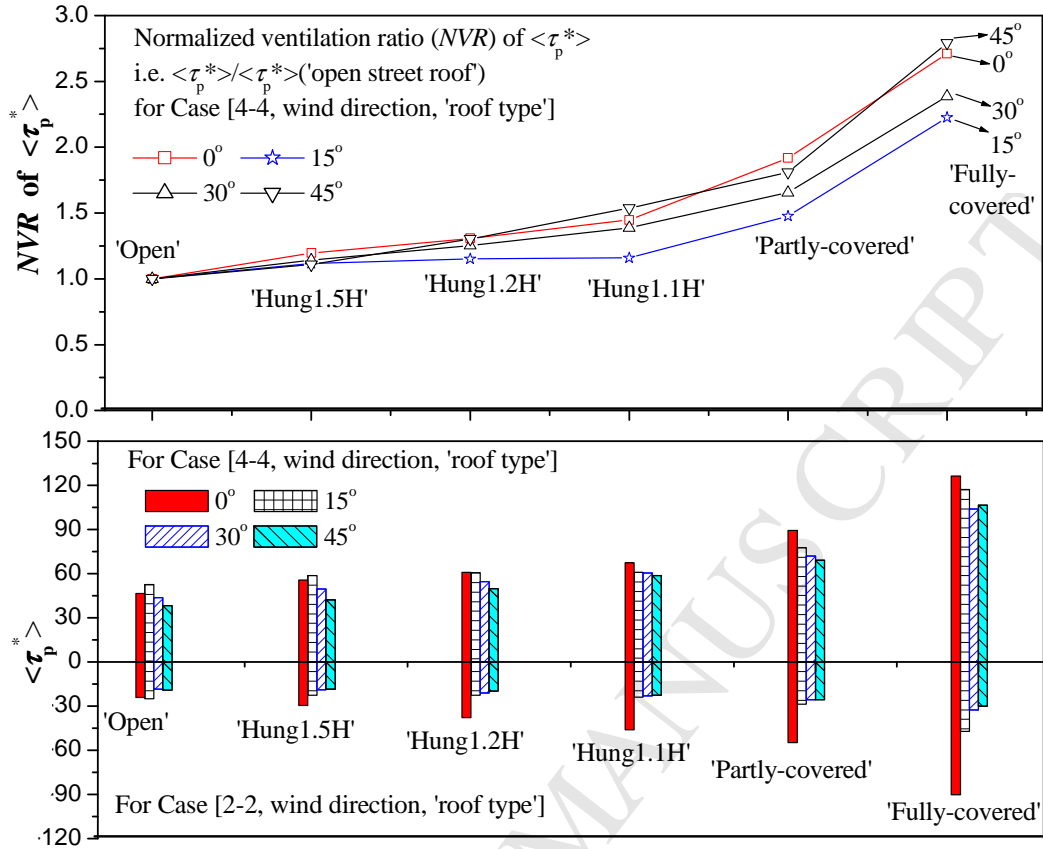
(b)



(c)

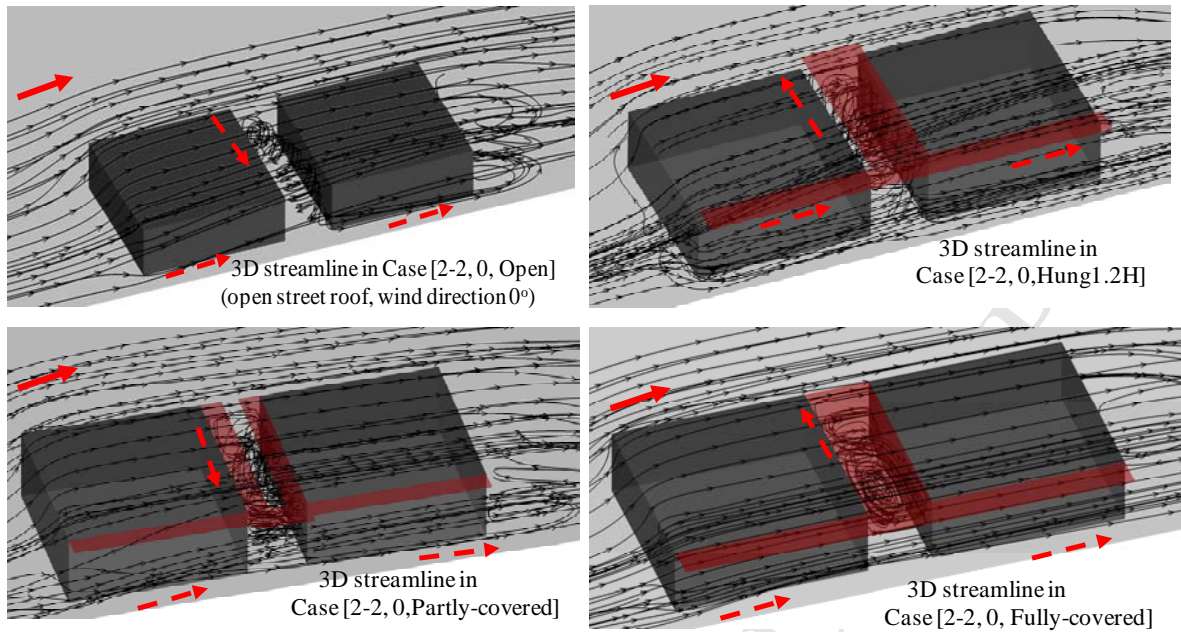


(d)

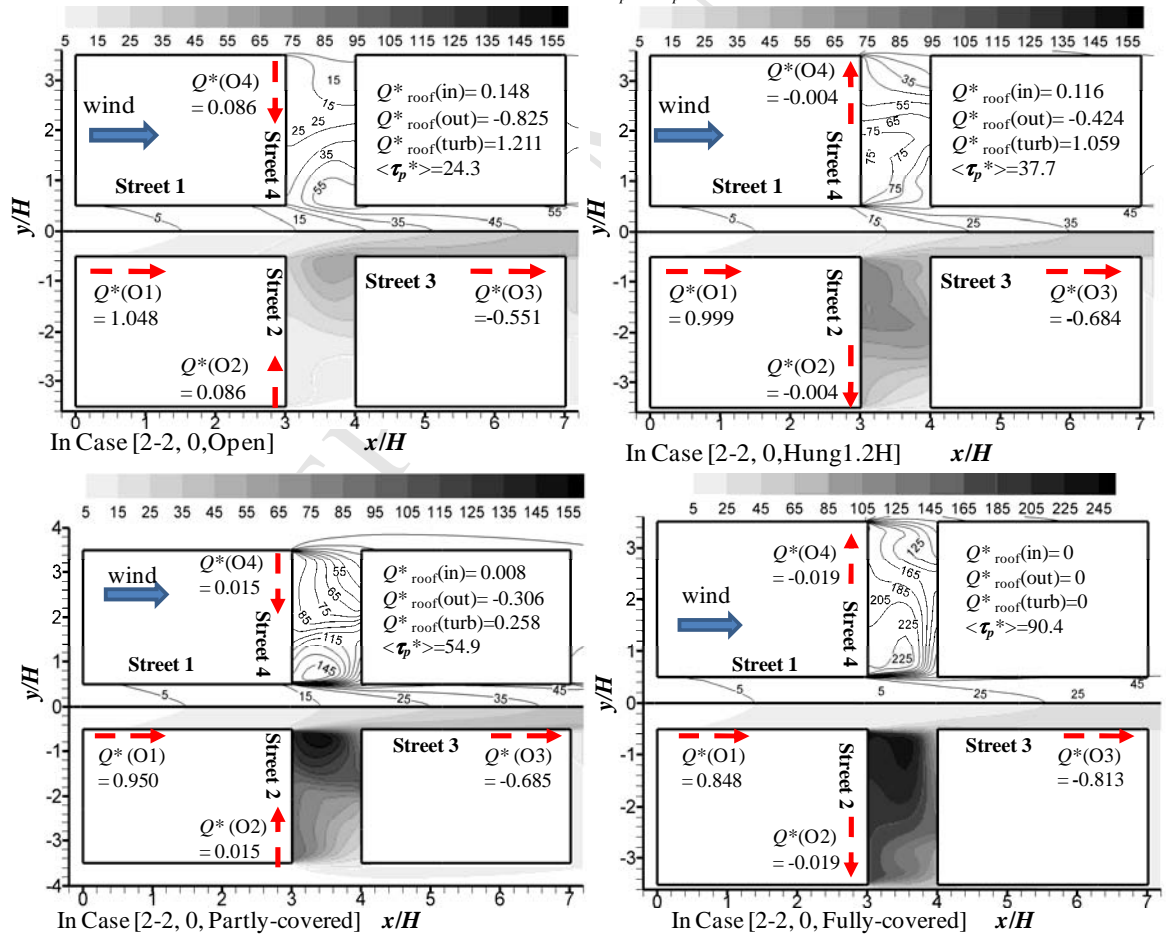


(e)

Fig. 13 Hang et al.

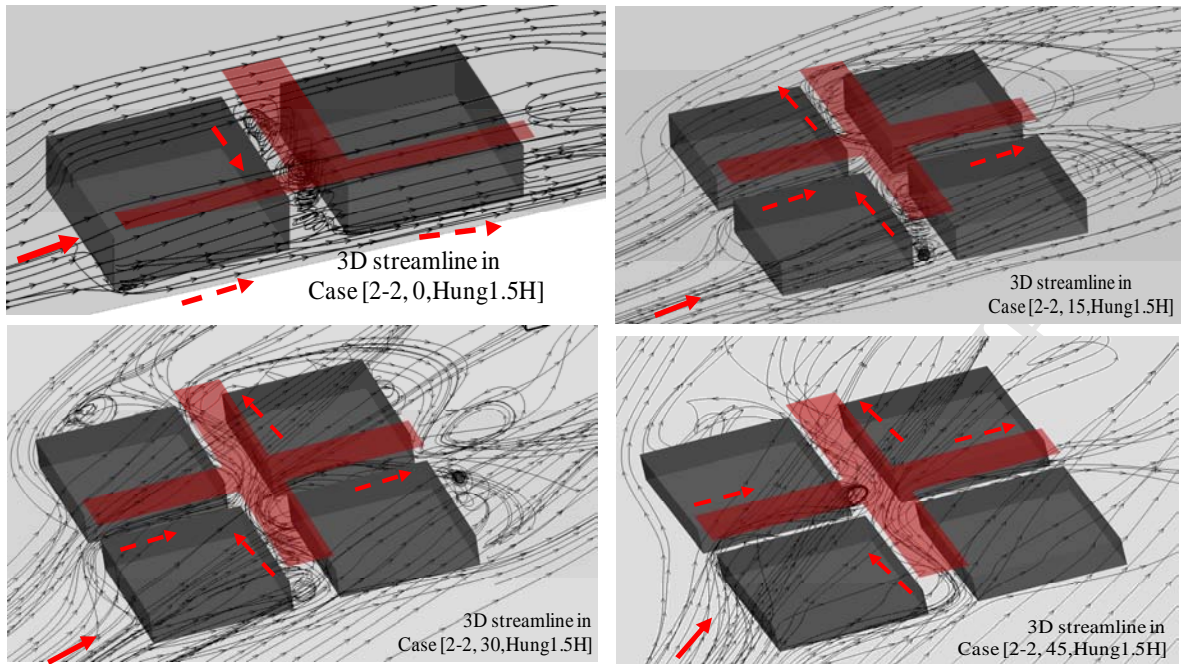


(a)

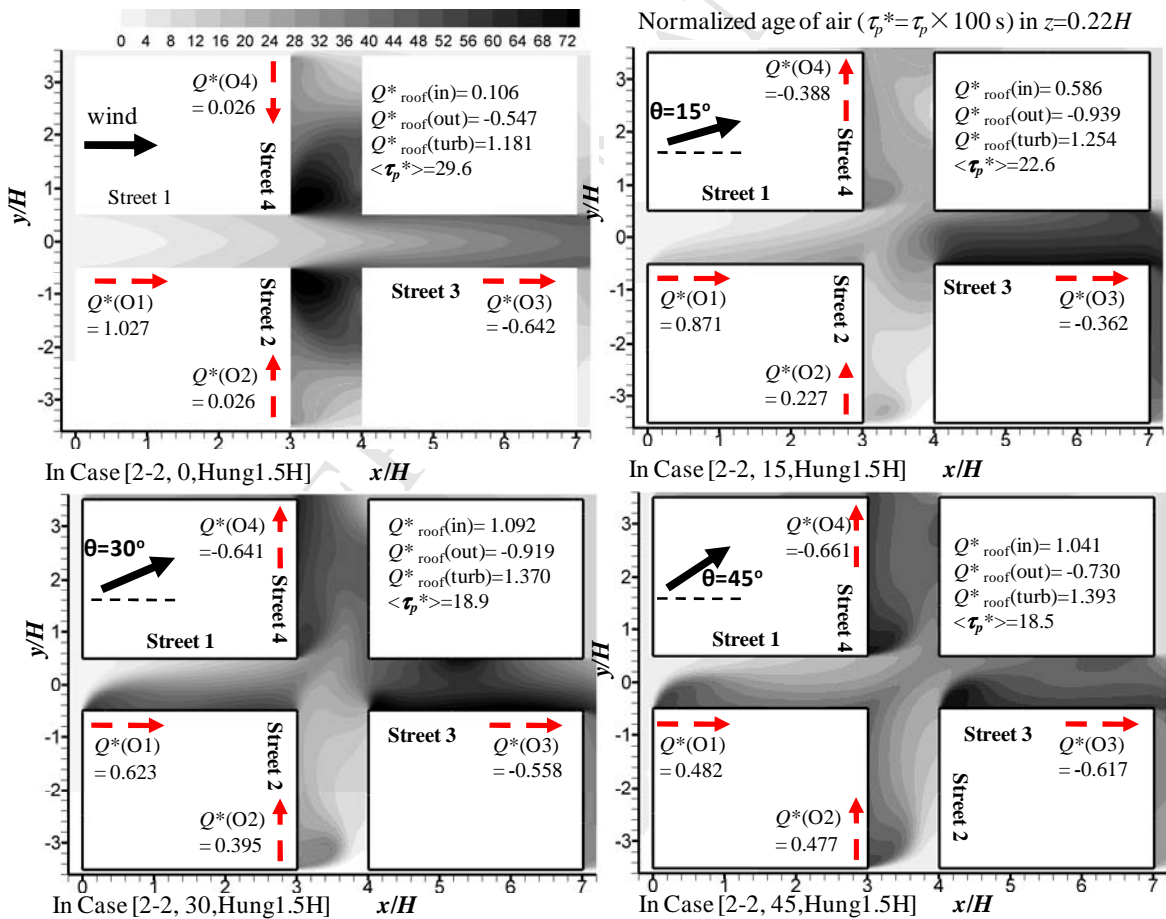
Normalized age of air ($\tau_p^* = \tau_p \times 100$ s) in $z=0.22H$ 

(b)

Fig. 6 Hang et al.

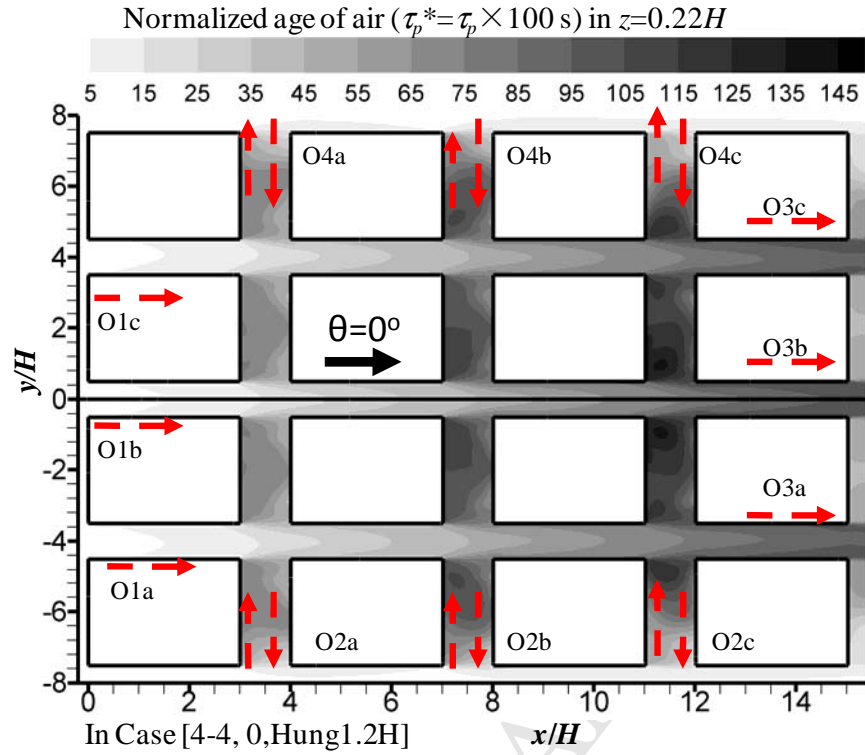


(a)

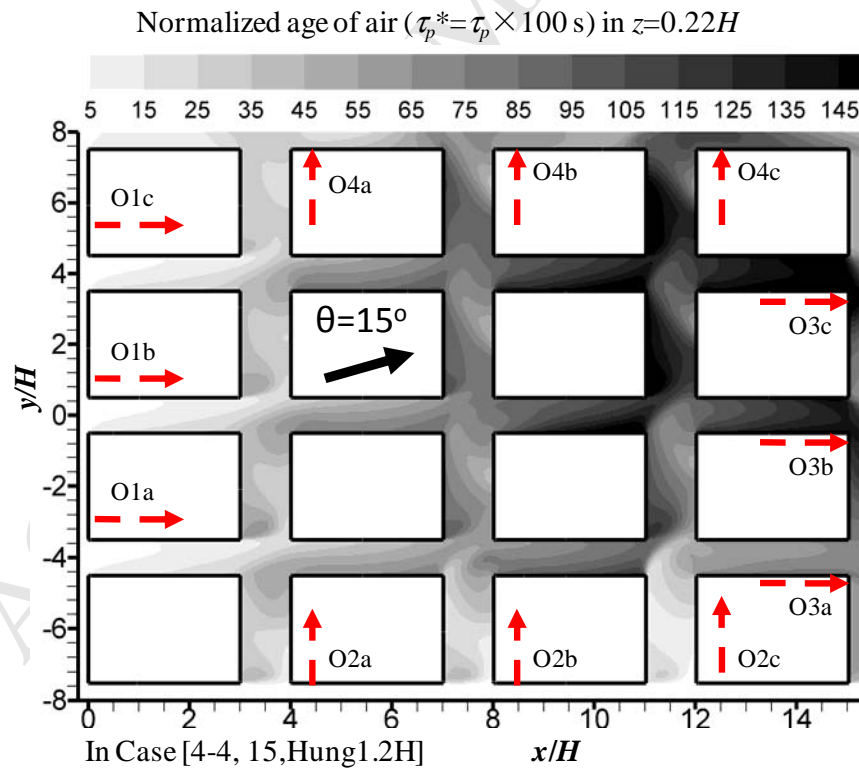


(b)

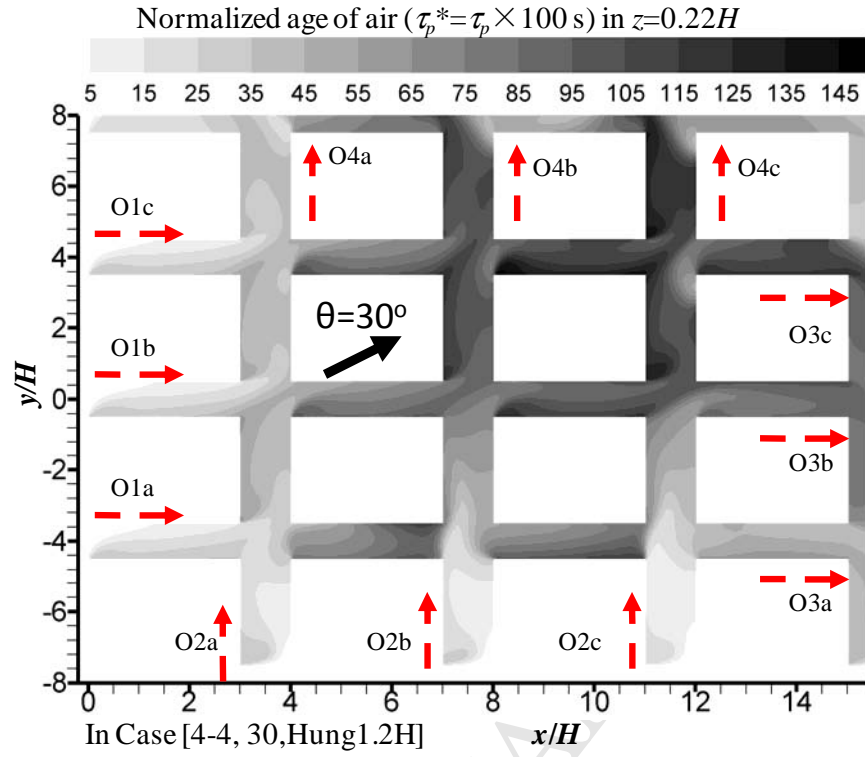
Fig. 7 Hang et al.



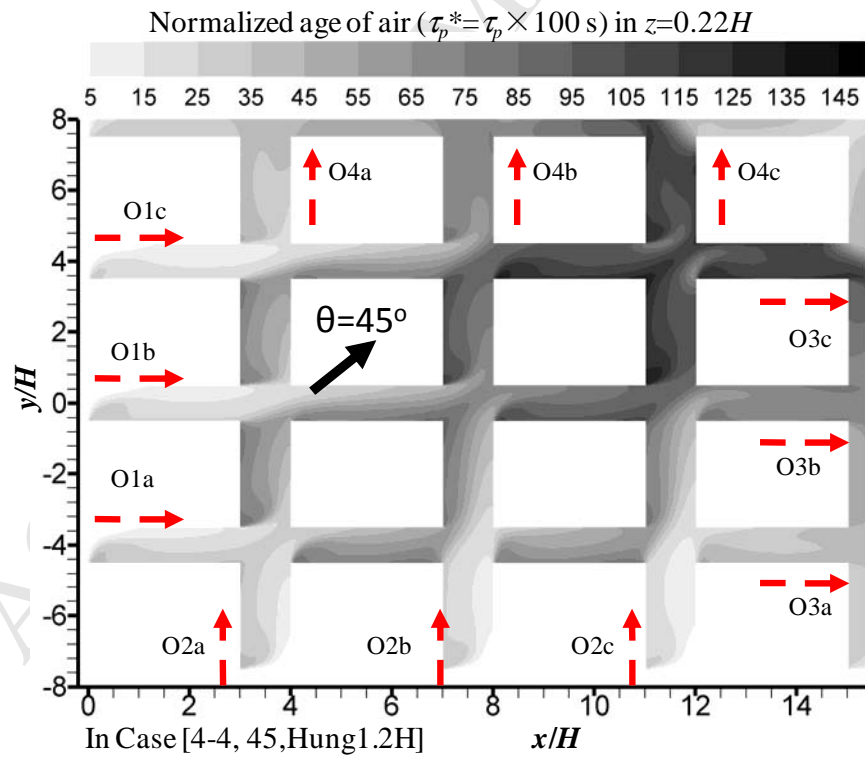
(a)



(b)



(c)



(d)

Fig. 10. Hang et al.